Biodegradable Silica-Based Nanoparticles with Improved and Safe Delivery of Protoporphyrin IX for the In Vivo Photodynamic Therapy of Breast Cancer

Zachary K. Lyles, Mubin Tarannum, Cayli Mena, Natalia M. Inada, Vanderlei S. Bagnato, and Juan L. Vivero-Escoto*

Silica-based nanoplatforms are highly versatile and attractive delivery systems for cancer treatment. These platforms have been used for the effective delivery of pharmacological agents in preclinical settings. Though silicon oxide is found naturally in the human body, a major limitation associated with silica-based nanoparticles is their slow biodegradability. Therefore, the potential risks related to the longer bioaccumation of these materials can be significant. In this work, the synthesis and application of a novel silica-based nanoplatform, polysilsesquioxane nanoparticles (PSilQ NPs) is reported. The developed PSilQ material contains stimuli-responsive properties, and improves biodegradability for the efficient delivery of a clinically relevant photosensitizer, protoporphyrin IX. Herein, it is demonstrated that the PSilQ nanoplatform is biocompatible and exhibits enhanced biodegradability in an immune-competent mouse model. In addition, PSilQ NPs show phototherapeutic efficiency for reducing the tumor burden in an orthotopic model of triple-negative breast cancer. These results may pave the way for the future clinical evaluation of this silica-based nanoplatform.

1. Introduction

Over the last decades, delivery systems based on silicon oxide (silica) have attracted extensive interest for a broad spectrum of biomedical applications. The wide variety of existing silica-based nanomaterials, including solid, mesoporous, hollow, and hybrid, presents several advantages for drug delivery (e.g., ease of synthesis and scale-up, high surface area, tunable porosity, size distribution, and composition) along with the access to versatile surface functionalization.[1,2] Some of these nanoparticles have been used to encapsulate molecules and/or metallic nanoparticles.[3,4] Despite these advantages, there is no reported clinical use of silica-based nanoparticles for systemic delivery of therapeutic agents. Silica is "generally regarded as a safe (GRAS)" ingredient by the U.S. Food and Drug Administration;[5,7] nevertheless, a crucial challenge that needs to be addressed, in order to advance this platform for future clinical applications, is to enhance its rate of biodegradability in the human body.[2,8] The development of hybrid silica-based materials such as polysilsesquioxane nanoparticles (PSilQ NPs) is a promising step in this direction.[9,10] Moreover, by rendering stimuli-responsive properties to the silsesquioxane monomer, an increase in the biodegradability of the polymeric nanostructure can be expected.[7–9,11]

PSilQ NPs have been previously used for the efficient delivery of chemotherapeutic agents, photosensitizers (PSs), nucleic acids, and contrast imaging agents.[12–15] The PSilQ nanoplatform provides similar advantages as the other silica-based nanomaterials, but with the additional benefit of having both a high content of organic functionalities in the matrix and controlled degradability. Recently, the use of PSilQ platform has been investigated to improve the performance of light-activated treatments, such as photodynamic and photothermal therapy.[13] Photodynamic therapy (PDT) is an innovative, minimally invasive, and highly selective technique for the treatment of cancer, among other diseases.[16–18] PDT uses non-toxic PSs and oxygen, which upon activation with light of a specific wavelength triggers a photochemical process leading to the generation of reactive oxygen species (ROS) to eliminate cancer cells.[19,20] Some of the challenges associated with PDT include the increase of the PS concentration in the tumors and prevention of unwanted phototoxic side effects.[21,22] Currently, most clinically approved PSs belong to the porphyrin

Dr. Z. K. Lyles, M. Tarannum, C. Mena, Prof. J. L. Vivero-Escoto
Department of Chemistry
University of North Carolina Charlotte
Charlotte, NC 28223, USA
E-mail: jviveroe@uncc.edu

Dr. Z. K. Lyles, M. Tarannum
Nanoscale Science Program
University of North Carolina Charlotte
Charlotte, NC 28223, USA

Dr. N. M. Inada, Prof. V. S. Bagnato
University of São Paulo
São Carlos Institute of Physics
Group of Optics
São Carlos, São Paulo 13566-590, Brazil

Prof. J. L. Vivero-Escoto
Center for Biomedical Engineering and Science
University of North Carolina Charlotte
Charlotte NC 28223, USA
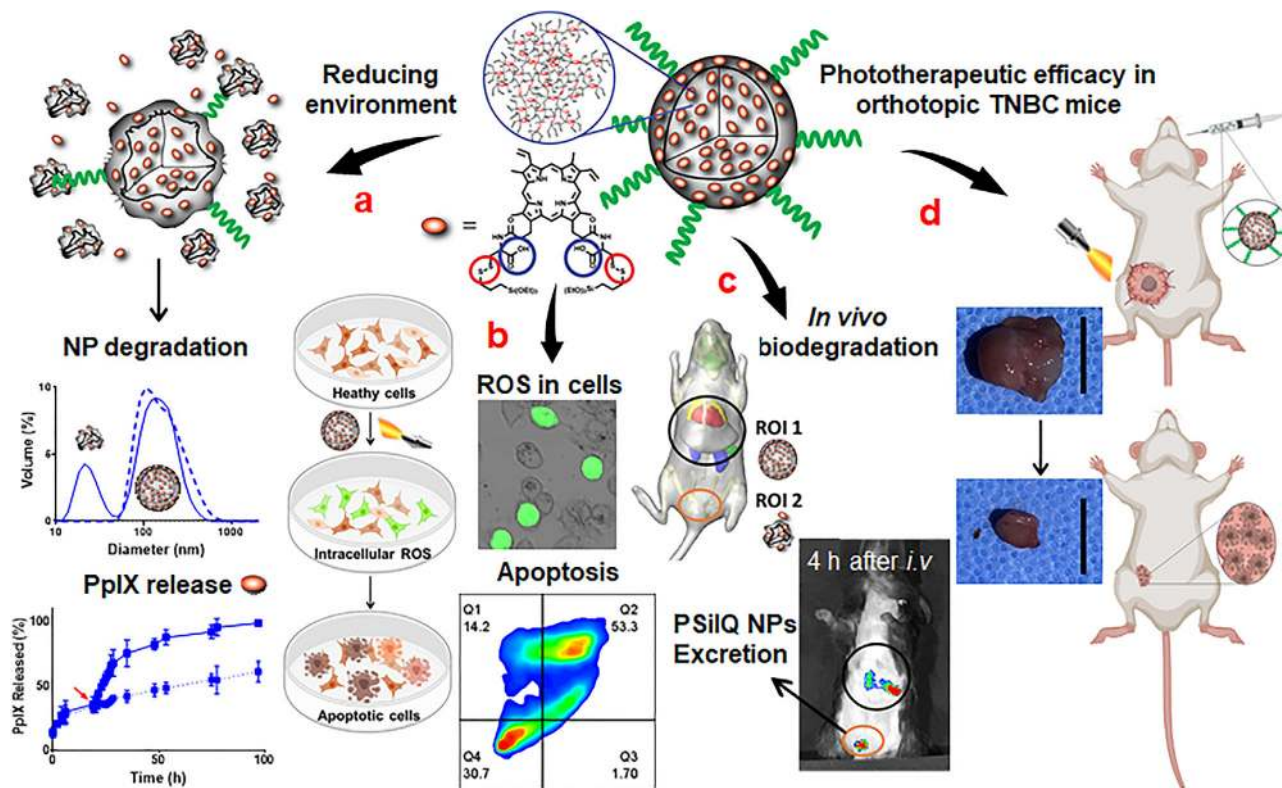
Scheme 1. Schematic representation of PSilQ NPs features and their in vitro and in vivo applications for the PDT of breast cancer. a) The redox-responsive PSilQ NPs exhibit enhanced degradability and PpIX release under reducing conditions. b) The PSilQ NPs show phototoxic effects through the generation of ROS causing cell apoptosis. c) The in vivo experiments in an immune-competent mouse model further proved the biodegradability of PEG-PSilQ NPs. d) The effective phototherapy of TNBC using PEG-PSilQ NPs was shown in an orthotopic mouse model. Scale bar = 5 mm. Illustrations created using BioRender.com.

or chlorin families, such as photofrin and protoporphyrin IX (PpIX), and its precursors including aminolevulinic acid (ALA) and methyl aminolevulinate (MAL).[19,20] Most of these compounds exhibit poor water solubility, thus posing a challenge for intravenous delivery. In addition, the PSs are not selective for the target tissue causing increased light sensitivity.[23,24] Nanoparticles increase the selectivity and stability of PSs while reducing unwanted side effects, such as dark toxicity and light sensitivity, which can enhance the overall PDT effect.[25] Our group and others have investigated the use of stimuli-responsive PSilQ platform to incorporate a high payload of PSs to improve PDT for cancer. Our group has reported on the use of redox-responsive PpIX-based PSilQ NPs to improve the PDT effect against cancer in vitro.[26–28] We recently expanded the application of PSilQ nanoplatform for the combinatorial treatment of triple-negative breast cancer (TNBC) using chemo, photo, and gene silencing therapies.[14] Khashab and co-workers have also demonstrated the development of enzymatically degradable PSilQ NPs for in vitro imaging.[29] Nevertheless, to the best of our knowledge, all the results reported for these stimuli-responsive PSilQ NPs have been obtained only under in vitro conditions.

Herein, we demonstrate, for the first time, the safety, biodegradability, and phototherapeutic efficacy of a stimuli-responsive PSilQ nanoplatform in vivo. Our nanoplatform consists of a redox-responsive PpIX silane derivative as the

monomeric building unit (**Scheme 1**). The PSilQ NPs were fabricated using reverse microemulsion method and the surface of the PSilQ NPs was modified with polyethylene glycol (PEG) to render stealth properties for in vivo delivery.[30] The physicochemical properties of the materials were thoroughly characterized. We demonstrated the degradability of PSilQ NPs and release of PpIX in solution under reducing environments. The phototoxic effect of PSilQ NPs, associated with the generation of ROS, was successfully proven in a panel of breast cancer cells. More importantly, in vivo experiments in a mouse model demonstrated that the PEG-PSilQ NPs are biodegraded and excreted without any adverse side effects. In addition, the PEG-PSilQ NPs exhibited an enhanced phototherapeutic effect in an orthotopic model of TNBC. Our data demonstrate the enhanced biodegradability, safety, and phototherapeutic efficacy of PSilQ nanoplatform for the treatment of TNBC in preclinical settings.

2. Results and Discussion

2.1. Synthesis and Characterization of Redox-Responsive PpIX-Loaded PSilQ NPs

The fabrication of a PSilQ nanoplatform with enhanced degradation depends on the selection of organic moieties with stimuli-responsive features, which are incorporated into the
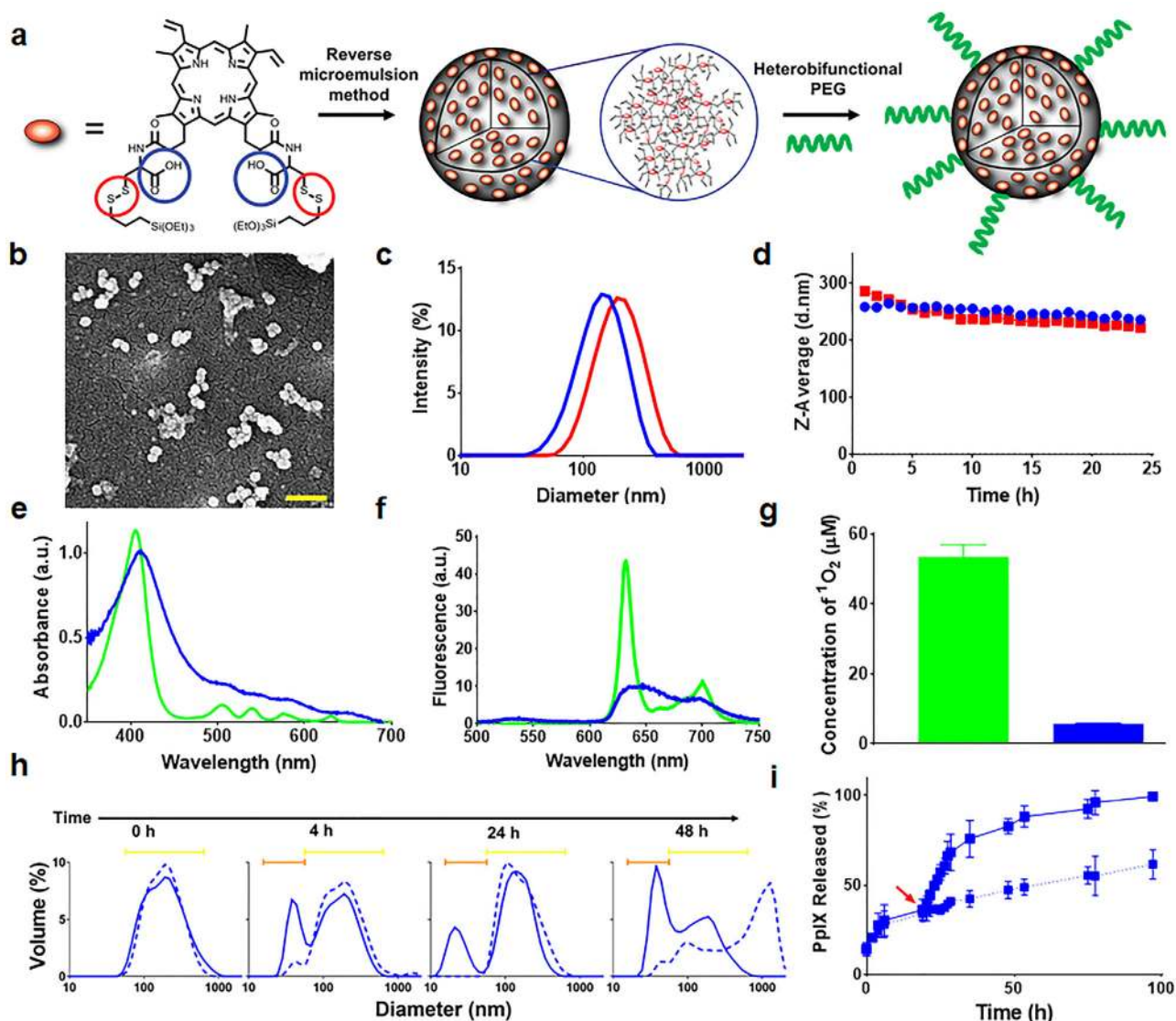
Figure 1. a) Schematic representation of the fabrication of PEG-PSilQ NPs. Silane derivative **1** is used as monomer for the fabrication of PSilQ NPs through a reverse microemulsion method. Further functionalization with heterobifunctional PEG polymer affords PEG-PSilQ NPs. Structural and photo-physical properties of PSilQ NPs. b) Representative SEM image of PSilQ NPs (scale bar = 200 nm). c) PSD plot of PSilQ (blue) and PEG-PSilQ (red) NPs in PBS (1×10^{-3} M) ($n = 3$). d) Colloidal stability of the PSilQ (blue) and PEG-PSilQ (red) NPs in complete cell culture media supplemented with serum for 24 h monitored using DLS. e,f) UV–vis and fluorescence spectra of PpIX (green) and PSilQ (blue) NPs (5×10^{-6} M PpIX). g) Generation of $^1O_2$ by PpIX (green) and PSilQ NPs (blue) under red light irradiation (570–690 nm, 30 s, 9 mW cm^{-2}) ($n = 3$). h) Time-dependent PSilQ NP degradation in solution under a reducing environment (DTT) monitored by DLS. PSD plots of PSilQ NPs in the presence (solid line) and absence (dashed line) of DTT (10×10^{-3} M) at different time points. The line gated in yellow indicates the original D_h, and the one in orange the new D_h ($n = 3$). i) Redox-responsive release of PpIX from PSilQ NPs in the presence (solid line) and absence (dashed line) of the reducing agent DTT ($n = 3$). The red arrow indicates the addition of reducing agent.

hybrid-inorganic framework.[2,9,10] We recently reported on the use of a redox-responsive PpIX silane ligand (**1**) to fabricate multimodal PSilQ nanoplatform. This ligand contains not only a disulfide bond that renders the redox-responsive properties, but also carboxylic acids for further chemical functionalization of the nanoparticles (**Figure 1**a). The synthesis of PpIX silane ligand (**1**) is carried out through a multi-step procedure as described previously by our group.[14] The fabrication of the PSilQ NPs was performed via a reverse micro-emulsion technique.[26] In this method, the micelles formed by the surfactant and

cosurfactant in the organic phase behaved as the nanoreactors containing an aqueous environment. We used a four-component approach for this reaction, consisting of Triton X-100 as the primary surfactant, hexanol as the cosurfactant, cyclohexane as the organic solvent, and water. The PpIX silane derivative (**1**) was dissolved into the water in the presence of ammonium hydroxide. The use of the base has two main purposes: first, to solubilize compound **1** in water by forming its carboxylate version; and second, to increase the rate of condensation of **1** inside of the nanoreactors to afford the desired PSilQ NPs.[1,15]

**ADVANCED
SCIENCE NEWS**

www.advancedsciencenews.com

**ADVANCED
THERAPEUTICS**

www.advtherap.com

Once the nanoparticles were fabricated, the nanoparticle surface was further functionalized with MeO-PEG-NH$_2$ (MW = 2 K) by the coupling reaction with the carboxylic acid groups exposed on the surface of the nanoparticles to afford PEG-PSilQ NPs (Figure 1a).

The structural properties of PSilQ and PEG-PSilQ NPs were characterized by using scanning electron microscopy (SEM), dynamic light scattering (DLS), and ζ-potential. SEM images show that the reverse microemulsion approach afforded spherical PSilQ NPs with diameters in the range of 37 ± 6 nm ($n = 160$) (Figure 1b; Figure S1, Supporting Information). DLS and ζ-potential measurements were performed in phosphate-buffered solution (PBS, 1×10^{-3} M, pH = 7.4) to determine the hydrodynamic diameter (D_h) and surface charge of the nanoparticles, respectively. PSilQ NPs exhibited a D_h of 139 ± 1 nm (PDI = 0.23) (Figure 1c) with a surface charge of -43 ± 3 mV ($n = 3$) (Table S1, Supporting Information). The D_h of the nanoparticles were larger than the diameter found by SEM, most likely due to slight aggregation and/or swelling of the PSilQ material in the solution, as previously reported.[31] The negative charge on the surface of the PSilQ NPs is due to the contribution of both silanol and carboxylate groups, which are produced after their deprotonation under physiological pH.[28] After functionalization with MeO-PEG-NH$_2$ polymer, the D_h of the nanoparticles increased to 196 ± 3 nm (PDI = 0.25) (Figure 1c) due to the passivation of the surface by the PEG polymer as corroborated by the slight increase in the surface charge to -38 ± 2 mV ($n = 3$) (Table S1, Supporting Information). The colloidal stability of both the PEG- and PSilQ NPs was evaluated in cell media containing fetal bovine serum during 24 h (Figure 1d). The data showed an increase in the D_h for both nanoparticles compared to the D_h in PBS, which is most likely due to the formation of a protein corona on the nanoparticle surface.[32] The D_h for both nanoparticles remained fairly constant during the whole experiment corroborating their colloidal stability in the presence of serum.[30]

The UV–vis spectra of PSilQ NPs clearly showed the characteristic Soret band for PpIX; however, the four Q-bands are not as well-defined as those of the parent molecule (Figure 1e; Figure S2a, Supporting Information). As we have reported before, a red shift from 405 to 413 nm for the Soret band of the PSilQ NPs was observed, which is indicative of the partial formation of J-aggregates associated with PpIX assembly in the PSilQ framework.[14] In addition, the presence of PpIX in the PSilQ NPs was corroborated by Fourier transform infrared spectroscopy (Figure S2b, Supporting Information). The broad stretching vibration at 3300–2800 cm^{-1} clearly demonstrated the presence of O—H bond associated to carboxylic acids; the vibrations at 2950–2800 cm^{-1} are indicative of C—H sp^3 bonds; the signal for the C=O group appears at 1690 cm^{-1}; two vibrations at 1445 and 1245 cm^{-1} associated with C=N and C—N due to the presence of PpIX are identified; and finally, the diagnostic vibrations for Si—O and Si—C bonds at 1100–900 cm^{-1} and 865 cm^{-1}, respectively, are also observed. The loading of PpIX molecules in the PSilQ and PEG-PSilQ NPs was determined through UV–vis spectroscopy. The amount of PpIX in the PSilQ and PEG-PSilQ NPs was determined to be 5.7 ± 2.2 and 4.2 ± 0.4 wt% respectively ($n = 5$). The loading of PpIX is similar to the one reported for other nanocarriers.[33–35]

The fluorescence of the PSilQ NPs drastically decreased when compared to PpIX (Figure 1f; Figure S2c, Supporting Information), which can be explained by the self-quenching effect occurring due to the close proximity of the PpIX molecules in the PSilQ framework.[26,36] A similar effect was observed when the production of $^1O_2$ was tested in solution. Molecular PpIX produced 53.5×10^{-6} M of $^1O_2$, whereas the PSilQ NPs, having a similar number of PpIX molecules, only produced 5.6×10^{-6} M of $^1O_2$ (Figure 1g). In this case, almost a 10-fold reduction in the generation of $^1O_2$ compared with PpIX was observed. Our group has previously used the self-quenching effect to rationally design stimuli-responsive systems where, once the PS agent is encapsulated in the nanoparticle, the generation of $^1O_2$ is drastically reduced.[14,26] Nevertheless, once the nanoparticles degrade in response to the intracellular stimuli releasing the molecular PS, the $^1O_2$ production is restored. This approach provides high selectivity to the PDT outcome reducing the side effects related to PSs.

The ability to develop stimuli-responsive nanoparticles that can release their cargo and be degraded upon a given stimuli is the next generation of smart materials for clinical applications. In this respect, internal stimuli, such as pH, redox potential, and up-regulated proteins, can be exploited as triggers.[37,38] In particular, the high reduction potential of cancer cells has been used to afford redox-responsive drug delivery systems.[39] It has been established that cancer cells present high concentrations of reducing agents (e.g., glutathione, 2×10^{-3}–10×10^{-3} M), which are 100–1000 times higher than those in extracellular fluids and normal tissues.[40,41] Our group has previously reported on the development of nanoparticulate redox-responsive systems for the delivery of drugs, contrast agents, and PSs.[14,15,26–28,42] In this work, the silsesquioxane monomer contains a disulfide linkage (Figure 1a) that endows the redox-responsive properties to the PSilQ nanoplatform. To evaluate the performance of the PSilQ material, we first investigated its degradability in solution in presence of a reducing agent, dithiothreitol (DTT). To have a better representation of the sample composition during the degradation process, the %volume particle size distribution was chosen.[43,44] The particle size distribution (PSD) plots in Figure 1h showed that 4 h after the addition of DTT, there is a decrease of the hydrodynamic diameter of 190 nm, with the appearance of a new peak at 20–38 nm. After 48 h, increased percentage of the smaller D_h (20–38 nm) was observed compared to the original D_h (190 nm). This is indicative that the nanoparticles are being degraded in the presence of the reducing agent. The control experiment in the absence of DTT showed minimal degradation of the nanoparticles, but higher aggregation after 24 h.

The redox-responsive PpIX release was also investigated in the presence of DTT (Figure 1i). The PpIX release plot showed slow leakage of PpIX from the nanoparticles before the addition of the reducing agent. However, immediately after the addition of DTT, a fast release rate of PpIX (0.6 µg PpIX h^{-1}) was observed in the first 10 h, followed by a slow release rate (0.1 µg PpIX h^{-1}) in the next 25 h, and finally a plateau was reached at longer times (>96 h). The half-life ($t_{1/2}$) for the release of PpIX was ≈23 h under reducing conditions for PSilQ NPs. The control sample in the absence of DTT showed a constant slow release rate of PpIX (0.08 µg PpIX h^{-1}), most likely due to the hydrolysis of the silica and amide bonds.[2,8] As expected, these results demonstrated

**ADVANCED
SCIENCE NEWS**

www.advancedsciencenews.com

**ADVANCED
THERAPEUTICS**

www.advtherap.com

that the use of disulfide bonds in the PSilQ framework is a successful strategy to develop biodegradable delivery systems that respond to a reducing environment.

2.2. In Vitro Cellular Internalization, Phototoxicity, and Cell Death Mechanism of PSilQ NPs in Breast Cancer Cell Lines

PpIX is clinically approved and one of the most commonly used porphyrins for PDT.[45] However, the intrinsically poor water solubility of PpIX presents a major challenge in systemic delivery and cellular internalization. Currently, ALA or MAL are used as the precursors for PpIX delivery; nevertheless, a few issues hinder this approach.[46] For instance, the PDT efficacy depends on the in situ synthesis of PpIX inside the cells. In addition, the delivery of PpIX precursors is not target specific, leading to increased amounts of precursor administration with a consequent enhancement in light sensitivity.[23,24] Therefore, current research endeavors focus on developing delivery systems that safely transport and deliver PpIX.[21,47] Our PSilQ platform is designed to effectively transport and deliver PpIX inside the cells, with the additional benefit of redox-responsive degradation capability.

In recent years, PDT has shown great potential for breast cancer treatment. Evidence based on the initial trials for chest wall recurrence, recent clinical trial on primary tumors, and a plethora of preclinical data support the use of PDT to treat breast cancer.[48] Moreover, PDT provides a full range of application for BC with stand-alone palliative end treatment and in combination with traditional approaches.[49,50] Nevertheless, to achieve the full potential of PDT, it requires safe and selective delivery of PS to BC tumors, which can additionally lead to an improved PDT effect. The PSilQ nanoplatform is a promising approach to reach these goals. In this section, we demonstrate the in vitro performance of PEG- and PSilQ NPs in a panel of BC cell lines.

2.2.1. Study of the Cellular Internalization and Intracellular Localization of PSilQ NPs in Cancer Cells

PS uptake by cancer cells is crucial for the effective performance of PDT since the generated ROS are short-lived molecules and can only act close in a range of nanometers away from the site of generation. In addition, the mechanism of PDT-related cell death is dependent upon subcellular localization.[51,52] Therefore, we first investigated the cellular internalization and subcellular localization of the PSilQ NPs in MDA-MB-231 cells with PpIX as a comparison. The internalization of the PEG- and PSilQ NPs was determined using flow cytometry and confocal microscopy (**Figure 2**). The flow cytometry results showed that both PSilQ and PEG-PSilQ NPs are efficiently internalized by MDA-MB-231 cells compared to PpIX. PSilQ NPs showed 77.0% ± 3.8% and 87.8% ± 4.3% PpIX-positive cells when incubated with 50 and 100 μg mL^{-1} of nanoparticles, respectively. In a similar way, PEG-PSilQ NPs were internalized with 61.1% ± 2.1% and 77.0% ± 3.3% of PpIX-positive cells at 50 and 100 μg mL^{-1}, respectively. In the case of PpIX, lower ($p < 0.0001$) values for the internalization were observed, 18.1% ± 2.4% and 33.4% ± 4.1% at the equivalent concentrations of PpIX used for the nanopar-

ticles. This corroborates the need of using a nanocarrier to efficiently transport PpIX inside the cells. We observed a significant variance ($p < 0.05$) comparing the cellular internalization of PEG- and PSilQ NPs. This contrast can be accounted for by the difference in the protein corona formed on nanoparticles with or without PEG on their surface, which may result in a different interaction with cells.[32] Contrary to PSilQ, PEG-PSilQ NPs should have less interaction with the proteins in the media due to the presence of PEG. To test this hypothesis, the internalization of the nanoparticles was carried out in the absence of serum. The flow cytometry data showed comparable internalization for both NPs, indicating that the formation of protein coronas is partially driving the higher uptake for PSilQ NPs (Figure S3, Supporting Information).

Confocal microscopy was performed in the presence of PEG- or PSilQ NPs to qualitatively investigate the cellular uptake of the nanoparticles in MDA-MB-231 cells. The overlay of confocal micrographs, which includes blue, red, and DIC channels that correspond to cell nuclei (Hoechst 33342 dye), PpIX fluorescence, and cell morphology, respectively, confirmed the internalization of both PEG- and PSilQ NPs (Figure 2b). No internalization was observed in the presence of PpIX molecule under the same conditions (Figure S4, Supporting Information).

The subcellular localization of the PS is a critical parameter that determines the cell death mechanism associated to PDT.[53] Two organelles, lysosomes and mitochondria, are commonly related to this process. The photodamage of both organelles usually leads to apoptotic cell death. In this work, lysosomes are a key organelle since PpIX-loaded nanoparticles are usually localized in this organelle as reported by our group.[27] The subcellular colocalization of the PEG- and PSilQ NPs with lysosomes was investigated using a lysosome tracking probe (Lysosome Green). The confocal micrographs show that both PEG- and PSilQ NPs are colocalized in lysosomal compartments, as observed from the merged images between the red and green channels (Figure 2c). We expect that the PSilQ materials will kill BC cells through the apoptotic pathway. It has been previously demonstrated that molecular PpIX follows this pathway.[54]

2.2.2. Phototoxicity of PSilQ and PEG-PSilQ NPs against a Panel of Breast Cancer Cells

To study the phototoxicity of PEG- and PSilQ NPs, the human breast cancer cell lines, MDA-MB-231 and MDA-MB-453 cells, which were derived from aggressive forms of TNBC cells; and MCF-7 cells that were obtained from breast cancer adenocarcinoma were used. The cells were inoculated with different concentrations of either PEG- or PSilQ NPs to determine the EC$_{50}$ under light and dark conditions (**Figure 3**a1–a3; Figure S5, Supporting Information, and **Table 1**). The cells were irradiated thrice with red light (630 nm), using an LED light source, for a total fluence of 88.2 J cm^{-2}. EC$_{50}$ values, after treatment with PSilQ NPs, were determined to be 0.8×10^{-6}, 1.2×10^{-6}, and $>5.0 \times 10^{-6}$ M for MDA-MB-231, MDA-MB-453, and MCF-7 cells, respectively. Concentrations were based on the equivalent amount of PpIX in the nanoparticles. In a similar way, EC$_{50}$ values after treatment with PEG-PSilQ NPs were found to be 1.0×10^{-6}, 1.4×10^{-6}, and $>5.0 \times 10^{-6}$ M for MDA-MB-231, MDA-MB-453,
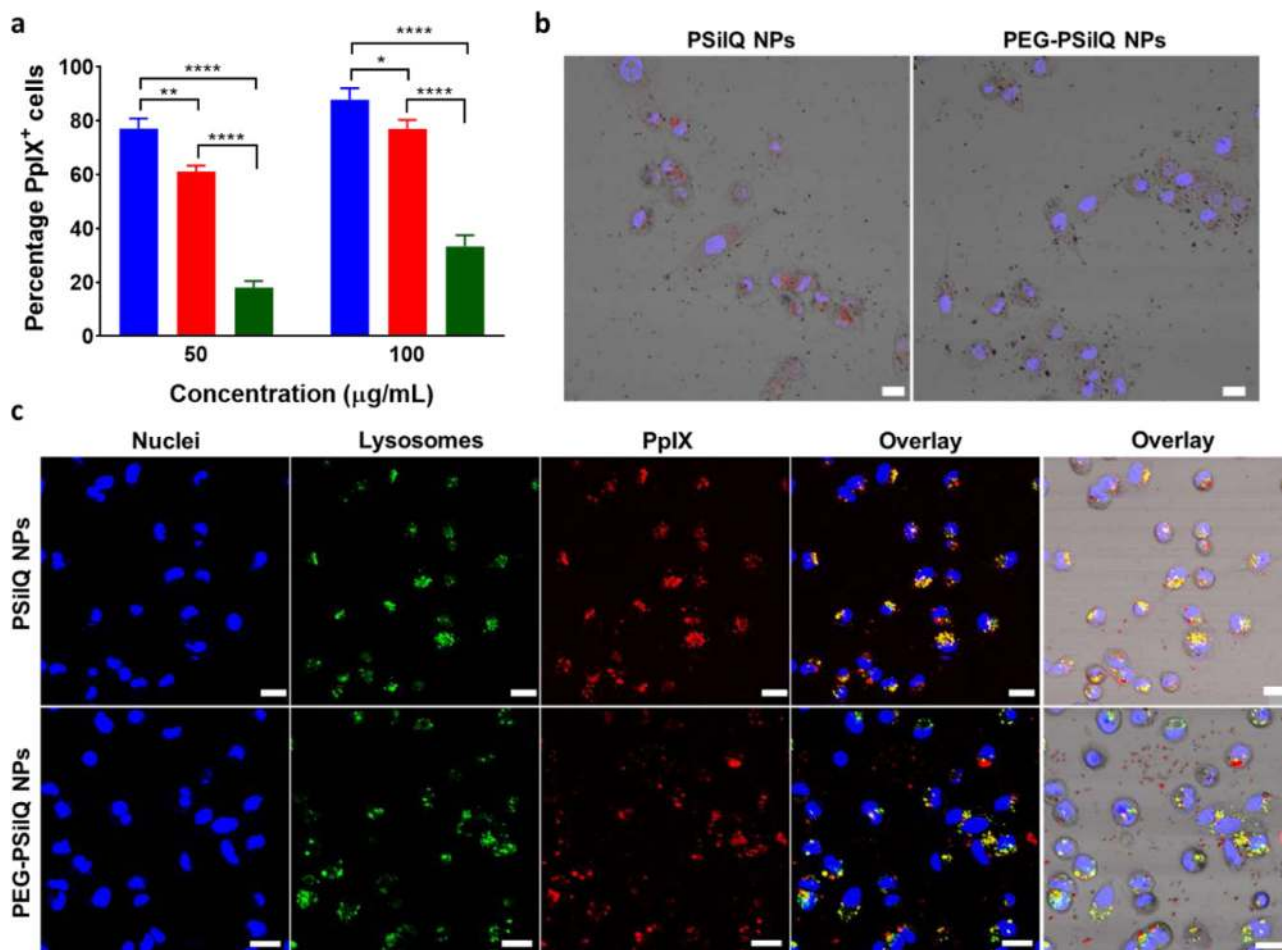
Figure 2. Cellular internalization and subcellular colocalization of PEG- and PSilQ NPs in MDA-MB-231 cells. a) Cellular uptake of PSilQ (blue) and PEG-PSilQ (red) NPs (50 and 100 µg mL^{-1}) in cells after 24 h of incubation in comparision with equivalent PpIX in media (green) evaluated using flow cytometry. Data represent the mean ± SD of three independent experiments. Statistics: One-way ANOVA using Tukey's multiple comparison test; ****$p \leq 0.0001$, ***$p \leq 0.001$, **$p \leq 0.01$, *$p \leq 0.05$, and ns: $p > 0.05$. b) Confocal images of cells after 24 h incubation with PEG- or PSilQ NPs (100 µg mL^{-1}). Scale bar = 20 µm. c) The colocalization of PEG- or PSilQ NPs with lysosomes was evaluated using confocal microscopy after 48 h incubation. The cell nuclei are observed in the blue channel after staining with Hoechst 33342 dye. Fluorescence in the FITC (green) channel indicates the staining of lysosomes (Lysosome Green), while fluorescence in the TRITC (red) channel indicates the presence of PpIX. The overlay of micrographs (yellow) shows the colocalization of lysosomes with PEG- or PSilQ NPs. Scale bar = 20 µm.

and MCF-7 cells, respectively. The difference observed in the EC$_{50}$ values for the nanoparticles, where PSilQ NPs are slightly more phototoxic than PEG-PSilQ NPs, is most likely due to the higher cellular uptake of the PSilQ NPs, as demonstrated in Section 2.2.1. Control experiments using PpIX molecule under same irradiation conditions showed EC$_{50}$ values of $>5.0 \times 10^{-6}$ M in all the cell lines, which indicates the lack of phototoxicity due to lower cellular uptake. Under dark conditions, both PEG- and PSilQ NPs showed very low cytotoxicity, in the panel of breast cancer cells, at the maximum concentration tested in this work (5×10^{-6} M PpIX) (Figure S5, Supporting Information). These results demonstrated that the PSilQ nanoplatform can efficiently transport and deliver PpIX inside breast cancer cells, with minimal dark toxicity and improved PDT effect. Several trends were observed for the phototoxicity of the PSilQ nanoplatform against breast cancer cells where the TNBC lines, MDA-MB-231 and MDA-MB-453, were more susceptible to the phototoxic effect

compared to MCF-7 cells. This observation has been previously reported for MDA-MB-231 and MCF-7 cells. The resistance of MCF-7 cells toward PDT is associated with the lack of expression of glutathione peroxidase 4 (GOX-4), which detoxifies lipid hydroperoxides.[55,56]

2.2.3. Study of the Intracellular Formation of ROS by PSilQ NPs

The intracellular generation of ROS is the important mediator in the photochemical cascade leading to photodamage and cell death after PDT.[51] Based on the efficient phototoxicity of the PSilQ nanoplatform in TNBC cells, we further evaluated the formation of ROS in MDA-MB-231 cells, after the treatment with PEG- and PSilQ NPs, using a dichlorofluorescein diacetate (DCFH-DA) assay. DCFH-DA is a non-fluorescent cell-
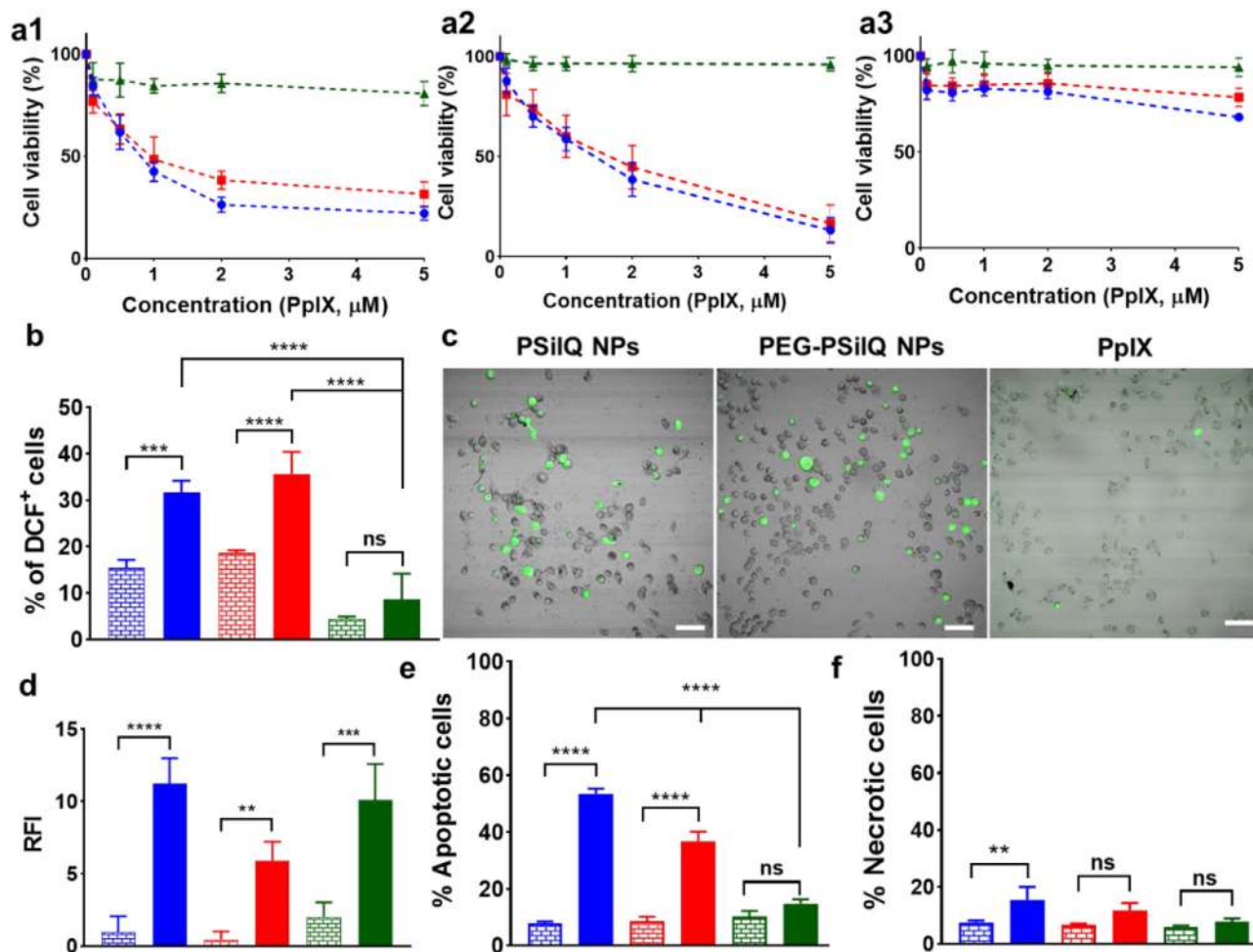
Figure 3. Phototoxicity and cell death mechanism of PEG- and PSilQ NPs in a panel of breast cancer cells. a) Cell viability plots of a1) MDA-MB-231, a2) MDA-MB-453, and a3) MC-7 cells after 72 h incubation, followed by three cycles of irradiation at 24.5 mW cm^{-2} for 20 min for a total fluence of 88.2 J cm^{-2} with various concentrations of PSilQ NPs (blue) and PEG-PSilQ NPs (red), and PpIX in media (green) ($n = 6$). b) Intracellular ROS generation was evaluated using DCFH-DA probe in MDA-MB-231 cells. Quantification of DCF positive cells is reported using flow cytometry after light irradiation (solid bars) compared to the samples in dark (brick-patterned bars). The cells were treated with 2×10^{-6} M PpIX equivalent of PSilQ (blue), PEG-PSilQ (red) NPs, or PpIX (green) for 24 h and irradiated with red light (630 nm, 24 mW cm^{-2} for 20 min). c) Confocal microscopy was used to qualitatively determine the intracellular ROS production in MDA-MB-231 cells using the DCFH-DA probe. The cells were treated with the equivalent PSilQ or PEG-PSilQ NPs or PpIX (2×10^{-6} M PpIX) for 24 h, followed by irradiation of red light in the presence of the DCFH-DA probe. Green fluorescence shows the generation of ROS (scale bar = 60 μm). d) The quantification of singlet oxygen was carried out using the SOSG probe. The cells were incubated with PSilQ (blue), PEG-PSilQ (red) NPs, or PpIX (green) (2×10^{-6} M PpIX) for 48 h and irradiated with red light (630 nm, 24 mW cm^{-2} for 20 min). The fluorescence quantified after light irradiation (solid bars) compared to the samples in dark (brick-patterned bars). Analyses of cell death mechanisms e,f) after phototherapy using PSilQ NPs in MDA-MB-231 cells. The cells were incubated with PSilQ NPs (blue) and PEG-PSilQ NPs (red), and PpIX in media (green) for 48 h, followed by three cycles of irradiation at 24.5 mW cm^{-2} for 20 min for a total fluence of 88.2 J cm^{-2}. The data are shown as the percentage of e) apoptotic and f) necrotic cells after light irradiation (solid bars) compared to the samples in dark (brick-patterned bars). For all the experiments in this figure, the data are represented as the mean ± SD of three independent experiments. Statistics: One-way ANOVA using Tukey's multiple comparison test: ****$p \leq 0.0001$, ***$p \leq 0.001$, **$p \leq 0.01$, *$p \leq 0.05$, and ns: $p > 0.05$.

Table 1. EC$_{50}$ ($\times 10^{-6}$ M) values for the phototoxicity of a panel of breast cancer cells.

Cell line	PSilQ NPs (D)	PSilQ NPs (L)	PEG-PSilQ NPs (D)	PEG-PSilQ NPs (L)	PpIX (D)	PpIX (L)
MDA-MB-231	>5.0	0.8	>5.0	1.0	>5.0	>5.0
MDA-MB-453	>5.0	1.2	>5.0	1.4	>5.0	>5.0
MCF-7	>5.0	>5.0	>5.0	>5.0	>5.0	>5.0

**ADVANCED
SCIENCE NEWS**

www.advancedsciencenews.com

**ADVANCED
THERAPEUTICS**

www.advtherap.com

permeable probe that is cleaved by cellular esterases to form DCFH. This molecule is oxidized to a highly green fluorescent dichlorofluorescein (DCF) probe by intracellular ROS.[57] To quantify the percentage of cells positive for DCF, MDA-MB-231 cells were incubated with PSilQ NPs, PEG-PSilQ NPs, or PpIX, followed by irradiation using red light (630 nm; 29.4 J cm^{-2}) in the presence of DCFH-DA. Flow cytometry data showed that the cells treated with PSilQ or PEG-PSilQ NPs have 35.1% $\pm$ 5.2% and 31.9% $\pm$ 3.4% of DCF-positive cells after light irradiation, respectively, which are higher ($p < 0.0001$) compared to the samples with no irradiation. These results indicated that ROS are efficiently generated in the presence of PSilQ NPs (Figure 3b). Cells treated with PpIX were evaluated under similar conditions, which showed only 8.9% $\pm$ 3.4% of DCF-positive cells, which is lower ($p < 0.0001$) compared to the nanoparticles.

The intracellular ROS production was further corroborated by confocal microscopy. As visualized by the confocal micrographs (Figure 3c), greater numbers of cells exhibiting green fluorescence due to DCF formation was associated with samples treated with PSilQ or PEG-PSilQ NPs after irradiation. These results successfully demonstrated that the PSilQ nanoplatform efficiently generate intracellular ROS upon irradiation.

To investigate, specifically, the intracellular production of singlet oxygen ($^1O_2$), we utilized an indirect method employing the singlet oxygen sensor green (SOSG) probe.[58] SOSG is a cell-impermeable compound that emits a strong green fluorescence after reacting exclusively with $^1O_2$.[59] For this experiment, we treated MDA-MB-231 with PSilQ NPs, PEG-PSilQ NPs, or PpIX and lysed the cells after treatment. Cell lysates were irradiated with red light (630 nm; 29.4 J cm^{-2}) in the presence of SOSG probe. The cells were washed thoroughly before lysis to ensure that only the internalized nanoparticles or internalized PpIX contributed to the $^1O_2$ quantification. Cells treated with PSilQ NPs or PEG-PSilQ NPs after light irradiation resulted in 11.2 $\pm$ 1.7 and 5.9 $\pm$ 1.3 fluorescence intensity, relative to control cells. These data were found to be significantly higher compared to cells treated with the NPs but not irradiated ($p < 0.0001$ and $p < 0.01$, respectively) (Figure 3d). In this experiment, PpIX molecules also generated a similar fluorescence intensity as the nanoparticles, which is most likely due to the PpIX aggregates being tightly bound to the cell surface. These results confirmed that intracellular ROS are efficiently produced by the nanoparticles upon light irradiation, resulting in a high phototoxic effect.

2.2.4. Determining the Mechanisms of Cell Death Triggered by PEG- and PSilQ NPs

PDT can induce cell death mainly via apoptosis, necrosis, and/or autophagy, which mechanism is favored depends on the PS type, its subcellular location, and treatment doses.[60–62] Subcellular localization of PSs in lysosomes and mitochondria primarily lead to apoptosis, whereas localization in the plasma membrane lead to necrosis. In particular, apoptosis and necrosis have been linked to the phototoxic effect of PpIX.[63] We hypothesized that the PSilQ nanoplatform would kill TNBC cells through an apoptotic pathway based on its subcellular localization in the lysosomes. To prove this idea, we used the Annexin V-FITC/propidium iodide

(PI) double staining assay after treatment of MDA-MB-231 cells with PSilQ NPs. The appearance of phosphatidylserine residues on the surface of the cell is an early event in apoptosis. Annexin V has a strong affinity for phosphatidylserine and it is used as a probe for staining apoptotic cells.[64] MDA-MB-231 cells were incubated with PSilQ, PEG-PSilQ NPs, or PpIX, followed by three cycles of irradiation at 24.5 mW cm^{-2} for 20 min for a total fluence of 88.2 J cm^{-2}. The cells were stained with Annexin-V-FITC/PI and analyzed using flow cytometry. PI is a cell-impermeable nuclear dye that does not stain early apoptotic or live cells due to the intact membrane. In late apoptosis and necrosis, the permeability of the cell membrane decreases, allowing the PI to enter the cells and interact with the nuclei.[65] The treated cell populations were classified as apoptotic, which includes both early and late apoptosis, and necrotic. The cells treated with PSilQ NPs and irradiation showed the highest presence of apoptotic cells (53.4% $\pm$ 1.8%), followed by PEG-PSilQ NPs (36.8% $\pm$ 3.3%), which both are higher ($p < 0.0001$) than samples not irradiated (Figure 3e). Cells treated with PpIX and irradiated with light did not show any significant difference compared with the control samples in dark conditions (14.8% $\pm$ 1.4% vs 9.5% $\pm$ 1.3%). A minimal percentage of cells, 15.5% $\pm$ 4.5% and 11.8% $\pm$ 2.5%, underwent necrosis after treatment with PSilQ ($p < 0.01$) or PEG-PSilQ NPs ($p > 0.1$), respectively. These data confirmed our hypothesis that the PSilQ nanoplatform killed TNBC cells through the apoptosis pathway. We do not rule out the possibility that other cell death mechanisms, such as autophagy, can play a role in the phototoxicity attributed to PSilQ NPs. However, an in-depth investigation of these mechanisms is out of the scope of this work.

2.3. In Vivo Biocompatibility and Biodegradability of PEG-PSilQ NPs

The degradability and safety of nanoparticulate delivery systems are critical factors for their clinical translation. The toxicity of silica-based materials for systemic administration has been extensively investigated in preclinical settings. Our group and others have reported that silica-based nanoparticles are biocompatible.[8,66–68] Though silica nanoparticles are safe, the slow degradation and excretion of this material is a limitation that can hamper its future translation into the clinic. It has been reported that silica-based materials can take weeks to be excreted from the animal body.[2,7,66,68] Different approaches have been explored to enhance the biodegradability of these materials. In particular, the incorporation of stimuli-responsive linkers in the framework of the nanoparticle have been an attractive strategy.[8,11] We hypothesize that the degradability of the PSilQ nanoplatform can be increased by rendering redox-responsive abilities to its framework.[9,10] Recent reports have shown the use of this approach for the delivery of platinum-based drugs and Gd-based MRI contrast agents in vivo.[12,15] Nevertheless, there is no precedent of any report in preclinical settings of the use of biodegradable PSilQ NPs for the delivery of PSs.

The safety and biodegradability of PEG-PSilQ NPs was first evaluated in immune-competent C57BL/6 mice. As a control material to compare the biodegradability of PEG-PSilQ NPs, we used mesoporous silica nanoparticles (MSNs) of a similar size (47.2 $\pm$ 3.9 nm). The synthesis and characterization of the MSNs

used in this work are described in the Supporting Information (Figure S6 and Table S2, Supporting Information). MSNs are selected for comparison because they are as widely used for drug delivery as PSilQ NPs. Moreover, MSNs also experience a similar slow degradability characteristic of silica-based platforms.[8,69]

To evaluate the safety and biodegradability of PEG-PSilQ NPs, different doses of the material (20, 40, and 60 mg kg^{-1}) were administered intravenously. PEG-MSNs (50 mg kg^{-1}) were also administered, through the same route, as the control group for biodegradability. NIR fluorescence was used to track both platforms' distribution in the mice by imaging the fluorescence in the abdominal region at 5, 30 min, 1, 4, 24, and 48 h post-injection. The data for PEG-PSilQ NPs (40 mg kg^{-1}) are shown as representative for the in vivo fluorescence analysis and quantification in comparison to PEG-MSNs (**Figure** 4a,b). We observed a trend where the fluorescence increased over time and reached a maximum at 4 h, followed by a decrease back to the background fluorescence at 24 h (Figure 4c). In comparison, the same analysis for the mice injected with MSNs showed a clear accumulation of the MSN material in the abdominal region as early as 30 min; and at 4 h, reaching a maximum fluorescence intensity that was an order of magnitude higher than the fluorescence intensity for PEG-PSilQ NPs (Figure 4b,c). There was only a slight decrease in the fluorescence after 24 h, indicating that the MSNs remained in the abdominal region even after 48 h. Previous reports have shown that MSN materials require a week or more to be completely excreted from the body and that they are usually excreted through the hepatobiliary pathway.[2,8]

To further investigate the kinetics of degradation associated with PEG-PSilQ NPs, we divided the ventral region of mice into two main regions of interest (ROI): ROI-1 focuses on the upper abdominal section, encompassing the liver, spleen, and lungs, while ROI-2 was chosen to include the bladder region in the lower abdomen (Figure 4d). The analysis of the PpIX fluorescence signals from ROI-1 and ROI-2 was carried out at different time points. It was evident that the PEG-PSilQ NPs accumulate in the ROI-1 as quickly as 30 min, but start to decrease after 4 h (Figure 4e). Interestingly, the fluorescence in the ROI-2 showed a trend in increased fluorescence after 1 h, which was maintained until 48 h. These results suggest that the PEG-PSilQ NPs may be excreted via the renal excretion pathway.[70] We hypothesize that the PEG-PSilQ NPs start to degrade in the presence of a strongly reducing environment affording smaller fragments with sizes below the threshold for the renal excretion. As demonstrated in section 2.1, that is the degradation outcome observed in solution. To further confirm the excretion pathway, a more rigorous pharmacokinetics study needs to be carried out.

The biodistribution of the PEG-PSilQ material was determined by analyzing the NIR fluorescence, PpIX, and Si element content in major organs. Mice injected with PEG-PSilQ NPs (20, 40, or 60 mg kg^{-1}) or PEG-MSNs (50 mg kg^{-1}) were euthanized 10 days post-intravenous injection. The major organs, including liver, lungs, kidneys, spleen, and heart, were imaged using the IVIS imaging system and the NIR fluorescence was quantified (Figure S7c,d, Supporting Information). The fluorescence from each organ associated to the different doses of PEG-PSilQ NPs is similar to the control group ($p > 0.05$). These results indicate that PEG-PSilQ NPs have most likely been excreted from the animal body after 10 days. In comparison, organs from mice in-

jected with the PEG-MSNs showed increased fluorescence. The accumulation of PEG-MSNs was higher than the control for liver ($p < 0.0001$), spleen ($p < 0.0001$), lungs ($p < 0.005$), and kidneys ($p < 0.01$) (Figure S7d, Supporting Information). The biodistribution of the PEG-PSilQ platform was further corroborated by analyzing the amount of Si element using ICP-OES in three organs, liver, kidneys, and lungs as these are the three most likely organs for the nanoparticles to accumulate. The levels of Si for the PEG-PSilQ platform in each organ, regardless of the initial dose (20, 40, or 60 mg kg^{-1}), are similar to the control mice organs ($p > 0.05$) (Figure 4f). Nevertheless, increased accumulation of Si associated to the PEG-MSNs in liver ($p < 0.001$) and lungs ($p < 0.005$) compared to the control group was observed. In the case of kidneys, the values were statistically similar to the other groups, which are not surprising considering that PEG-MSNs are usually excreted through the hepatobiliary excretion pathway. We also determined the amount of PpIX molecule in liver, lung, and kidneys using a fluorometric method.[71] The amount of PpIX molecule found in the organs for PEG-PSilQ NPs are similar ($p > 0.05$) to the control group (Figure 4g). It is important to point out that PpIX is ubiquitous in blood, which accounts for some of the high values of PpIX molecule detected for the control group. Together, all these results build a strong case that demonstrates the PEG-PSilQ nanoplatform is indeed excreted from the animal body after 10 days post-intravenous administration. Our data also show that the PEG-PSilQ NPs are excreted faster than PEG-MSNs, which supports our original hypothesis that by rendering redox-responsive properties, the biodegradability of the material is enhanced.

We monitored the weight of the mice every day for a period of 10 days post-intravenous injection to determine if the PEG-PSiQ NPs cause any toxic effects. There were neither adverse side effects nor weight loss observed during this time (Figure S8a, Supporting Information). Moreover, to further confirm the safety of PEG-PSilQ NPs, histological evaluation of major organs was performed (Figure S8b, Supporting Information). The H&E slides for the organ sections showed no signs of adverse effects. These data demonstrated that the PEG-PSilQ nanoplatform is safe at concentrations as high as 60 mg kg^{-1} during the time frame of our experiments.

2.4. Investigation of the Phototherapeutic Efficacy Using PEG-PSilQ NPs in an Orthotopic Mouse Model of TNBC

In addition to biodegradability and safety, a critical requirement for a nanoparticulate platform, in order to be used as an effective delivery system for PDT in vivo, is its effective therapeutic outcome. We investigated the phototherapeutic efficacy of PEG-PSilQ NPs in an orthotopic model of TNBC. Patients with TNBC are treated with conventional chemotherapy and radiation therapy, which mostly are ineffective and result in several side effects. Therefore, there is a clinical need to develop new therapeutic alternatives for the treatment of TNBC.[72] To evaluate the therapeutic ability of the NIR-labeled PEG-PSilQ platform against TNBC in vivo, we developed an orthotopic mouse model using NSG mice and MDA-MB-231 TNBC cells.[73] Orthotopic implantation of the TNBC cells in mammary fat pads gives organ-specific mi-
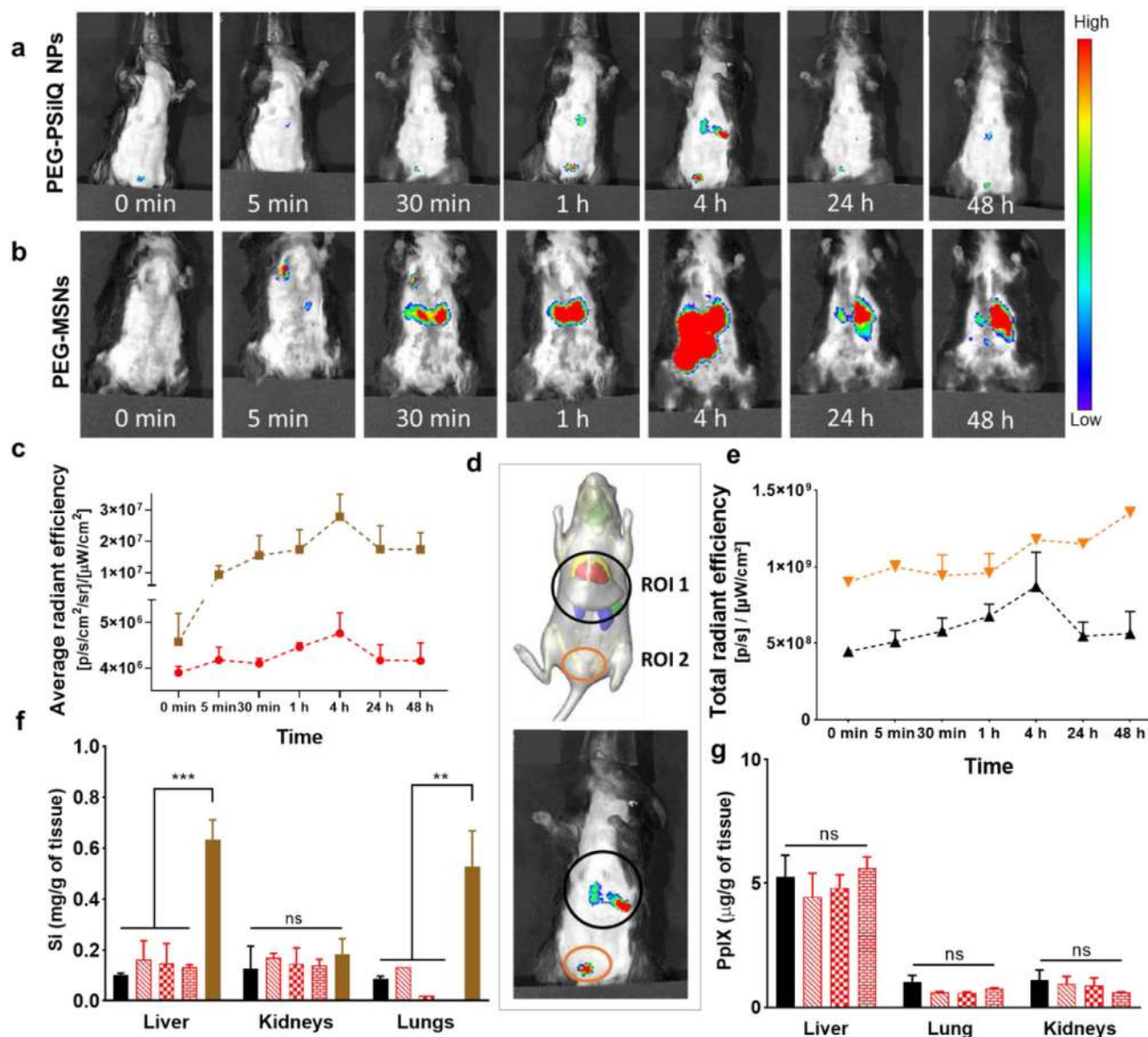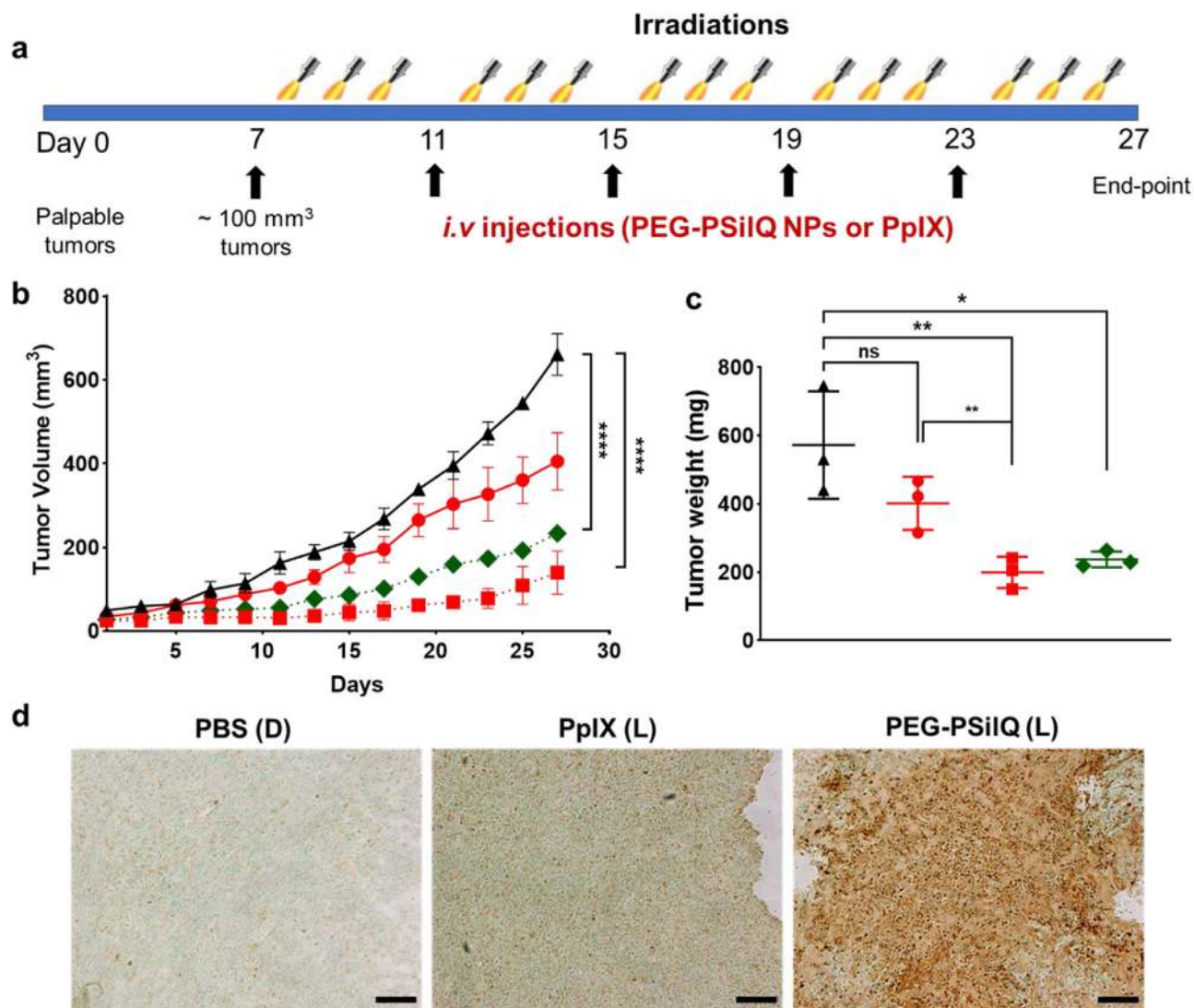
Figure 4. Biodegradability of PEG-PSilQ NPs and PEG-MSNs. Fluorescent signals captured by IVIS imaging system at different time points after intravenous injection with a) PEG-PSilQ NPs (40 mg kg^{-1}) and b) PEG-MSNs (50 mg kg^{-1}) in C57BL/6 mice. c) Quantification of the NIR fluorescence signal intensities in mice at different time points after intravenous administration with PEG-PSilQ (red circles) and PEG-MSN (brown squares) as analyzed using Living Image 4.5.5. d) Two different ROI were defined in the mouse body to analyze the kinetics of accumulation associated with nanoparticles: ROI-1 focuses on the upper abdominal region (liver, spleen, and lungs), while ROI-2 focuses lower and includes the bladder region. e) Quantification of the PpIX fluorescence signal in mice associated with ROI-1 (black upward triangle) and ROI-2 (orange downward triangle) at different time points after administration of PEG-PSilQ NPs, as analyzed using Living Image 4.5.5. f) Determination of the amount of Si element in liver, kidneys, and lungs harvested 10 days post-injection of PEG-PSilQ NPs at 20 mg kg^{-1} (red diagonal line pattern), 40 mg kg^{-1} (red checkers pattern), and 60 mg kg^{-1} (red brick pattern); and 50 mg kg^{-1} (brown solid) of PEG-MSNs. The control group of mice, which were not administered with nanoparticles, is represented by the black bars. g) Determination of the amount of PpIX in major organs harvested 10 days post-injection of PEG-PSilQ NPs at 20 mg kg^{-1} (red diagonal line pattern), 40 mg kg^{-1} (red checkers pattern), and 60 mg kg^{-1} (red brick pattern). $n = 3$ mice per group for all the figure sections. Statistics: Two-way ANOVA using Tukey's multiple comparison test; ****$p \leq 0.0001$, ***$p \leq 0.001$, **$p \leq 0.01$, *$p \leq 0.05$, and ns: $p > 0.05$.

croenvironments for primary tumor growth, progression of the disease, and metastasis.

To evaluate the phototherapeutic efficacy of the PEG-PSilQ nanoplatform, four groups were tested: PBS and PEG-PSilQ NPs without light irradiation, and PpIX and PEG-PSilQ NPs with light irradiation. The therapeutic regimen includes multiple administrations and irradiation times, as shown in **Figure 5**a. It has been previously shown that the effectiveness of PDT can be improved further through multiple exposures of light.[74] Mice bearing orthotopic MDA-MB-231 tumors of ≈100 mm^3 in size were intravenously injected with 50 mg kg^{-1} of PSilQ NPs, or with the equivalent amount of PpIX (2.1 mg kg^{-1} in PBS). The

**ADVANCED
SCIENCE NEWS**
www.advancedsciencenews.com

**ADVANCED
THERAPEUTICS**
www.advtherap.com

Figure 5. Phototherapeutic study of PEG-PSilQ NPs in the orthotopic TNBC mice. a) Schematic representation of the treatment regimen; the mice were injected intravenously with PEG-PSilQ NPs or PpIX five times (black arrows) and irradiated at 24, 30, and 48 h post injection. b) Tumor volume measurement throughout the study with various regimens: PBS (black triangles), PEG-PSilQ NPs (red circles), and PEG-PSilQ NPs (red squares) and PpIX (green diamonds) plus light irradiations ($n = 3$ mice per group). Two-way ANOVA using Tukey's multiple comparison test was performed between different groups and time points to determine the statistical difference. c) Tumor weights measured at the end point of the efficacy studies: PBS (black triangles), PEG-PSilQ NPs (red circles), and PEG-PSilQ NPs (red squares) and PpIX (green diamonds) plus light irradiations ($n = 3$ mice per group). Unpaired t-test was performed between different groups to determine the statistical difference. Statistics: ****$p \leq 0.0001$, ***$p \leq 0.001$, **$p \leq 0.01$, *$p \leq 0.05$, and ns: $p > 0.05$. d) Ex vivo analysis of tumor sections with TUNEL assay kit to show the apoptotic cells in the tumors after treatment with PBS without irradiations (D), and PpIX and PEG-PSilQ NPs with light irradiations (L). Scale bar = 200 μm.

tumor region was irradiated at 24, 30, and 48 h post-injection with red light (630 nm) for 12 min (90 J cm^{-2}) each time. The tumor growth was measured every other day using a caliper, and the tumor volume was plotted to determine the PDT efficacy on tumor burden (Figure 5b). The group treated with PEG-PSilQ NPs and light irradiation showed a statistically significant higher tumor growth inhibition ($p < 0.0001$) as compared with the PBS and PEG-PSilQ NPs without light irradiation. This is a clear indication that the PEG-PSilQ platform efficiently delivered photoactive PpIX molecule at the tumor site. Surprisingly, the group treated with PpIX and irradiated with red light also displayed a decrease rate in tumor growth ($p < 0.0001$) as compared with the

control group. The group treated with PEG-PSilQ NPs without light irradiation showed an inhibition ($p < 0.0001$) in tumor growth at the end of the experiment as compared with the PBS group; however, the two groups showed similar tumor growth until day 21. This result can be attributed to the fact that the mice, in all groups, were kept under cycles of light or dark with intervals of 12 h each as recommended by the IACUC. Most likely, this light environment triggered the phototherapeutic effect in the group threated with PEG-PSilQ NPs without light irradiation. After 20 days, the treatment was ended, mice were sacrificed, the tumors were excised, and tumor weights were measured. The weights corroborated the performance for the
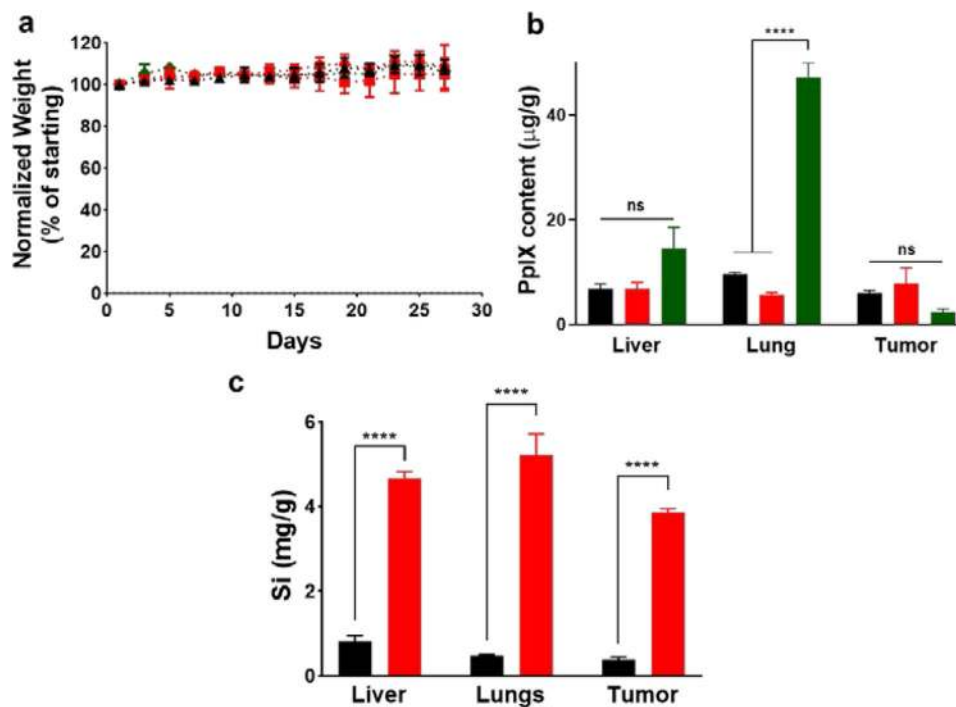
Figure 6. Posttreatment toxicity and biodistribution of PEG-PSilQ NPs in the TNBC orthotopic mouse model. a) Mice body weights were measured throughout the whole treatment; PBS (black triangles), PEG-PSilQ NPs (red circles), PEG-PSilQ NPs plus light irradiations (red squares), and PpIX plus light irradiations (green diamonds) ($n = 3$ per group). b) Determination of the amount of PpIX in liver, lungs, and tumor after treatment with PBS (black), PEG-PSilQ NPs (red), and PpIX (green) ($n = 3$ per group). Two-way ANOVA using Tukey's multiple comparison test was performed between different groups determine the statistical difference. c) Determination of the amount of Si element in liver, lungs, and tumor after treatment with PBS (black) and PEG-PSilQ NPs (red) ($n = 3$ per group). Statistics: One-way ANOVA using Tukey's multiple comparison test was performed between different groups determine the statistical difference. ****$p \leq 0.0001$, ***$p \leq 0.001$, **$p \leq 0.01$, *$p \leq 0.05$, and ns: $p > 0.05$.

irradiated PEG-PSilQ group as the tumor volumes for this group showed lower tumor weights ($p < 0.01$). The PpIX group also showed a similar therapeutic outcome ($p < 0.01$) as compared to the PBS group (Figure 5c). The group treated with PEG-PSilQ NPs in the absence of light showed a trend with smaller tumor weights, but it is not statistically different from the control group ($p > 0.05$). The phototherapeutic effect of the treatment with PEG-PSilQ NPs in tumor tissue was further investigated ex vivo using immunohistochemistry to determine the presence of apoptotic cells (TUNEL assay kit). This analysis revealed a higher population of apoptotic cells in the tumor tissue for the group treated with PEG-PSilQ NPs plus light, as is evident from the intense brown staining compared to both the group treated with PpIX plus light and the PBS group (Figure 5d). These results not only corroborate the effectiveness of PEG-PSilQ platform to kill MDA-MB-231 cells in vivo, but also demonstrate that apoptosis is the main mechanism for cell death.

2.5. Evaluation of Toxicity and Biodistribution of PEG-PSilQ NPs in the Orthotopic Mouse Model of TNBC

To account for any signs of adverse effects from the different treatments, the mice behavior was monitored, and the mice weights were measured every other day throughout the whole treatment period. No behavioral adverse effects were noted during the experiment. Moreover, the mice did not show any signif-

icant decrease in their body weights, indicating that neither the PEG-PSilQ NPs nor PpIX produced any significant adverse effects (**Figure 6**a). The histological examination of the H&E slides from the major organs of the mice treated with PEG-PSilQ NPs did not show any signs of toxicity as compared with the control group. Though we observed a high accumulation of PpIX in liver and lungs associated to the PpIX group (see below), no major signs of toxicity were detected on the H&E slides. It has been reported that PpIX can lead to biliary stones, hepatobiliary damage, and even liver failure, but these effects are usually observed only after long-term exposure (Figure S9c, Supporting Information).[75]

To determine the biodistribution of the PEG-PSilQ NPs after the treatment, the tumors and major organs including heart, spleen, kidneys, lungs, and liver were imaged for PpIX fluorescence using the IVIS imaging system (Figure S9a, Supporting Information). The quantification of PpIX fluorescence signals associated to the PEG-PSilQ NPs for all the organs is similar ($p > 0.05$) to the control group (Figure S9b, Supporting Information). This gives a good indication that most of the PpIX carried by the PEG-PSilQ platform has been cleared within the treatment period. However, the fluorescence signals for the group treated with PpIX molecule showed a significant accumulation of PpIX in liver and lungs ($p < 0.0001$) compared to both the nanoparticles and the control group. To confirm this observation, the PpIX content was quantified in liver, lungs, and tumor by using the fluorometric method after extraction of PpIX from

**ADVANCED
SCIENCE NEWS**

www.advancedsciencenews.com

**ADVANCED
THERAPEUTICS**

www.advtherap.com

those organs (Figure 6b). The higher accumulation ($p < 0.0001$) of PpIX molecule in both liver and lungs for the PpIX group was confirmed. The accumulation of PpIX molecules in these organs can be explained by the aggregation of the compound under physiological conditions. On the contrary, the amounts of PpIX in liver and lungs associated to the PEG-PSilQ NPs group were equivalent to the control group (Figure 6b). The presence of a high content of PpIX in the body has been associated with skin photosensitivity, biliary stones, hepatobiliary damage, and even liver failure, therefore necessitating the development of efficient delivery systems for PpIX. The Si content analysis from liver, lung, and tumor for the PEG-PSilQ NPs group confirmed the presence of nanoparticles in these organs (Figure 6c). These results point to the conclusion that PEG-PSilQ platform efficiently transport and deliver PpIX molecules to the tumor tissue, avoiding significant accumulation in other organs.

3. Conclusions

In this work, we report on the development of a silica-based redox-responsive polysilsesquioxane nanomaterial with improved biodegradability and safe delivery of PpIX. We show that PEG-PSilQ NPs have an effective phototherapeutic effect for the treatment of TNBC in vivo. Our data demonstrate that the redox-responsive PSilQ platform is degraded and quickly excreted from the animal body, most likely via a renal excretion pathway. The effective PDT treatment of orthotopic TNBC tumors shows that PpIX is efficiently delivered into the tumor region without decrease in photoactivity. Our in vitro and in vivo data corroborate that cancer cells are eliminated mainly through the apoptotic cell death pathway. Overall, the data reported demonstrate that PEG-PSilQ NPs are a promising candidate for the safe and efficient delivery of PpIX to reduce tumor growth in preclinical settings. We envision that demonstration of the redox-responsive properties of PSilQ NPs, which leads to their enhanced biodegradability and to effective delivery of the PS agent in the tumor site, will further advance the use of this platform for the treatment of cancer using PDT.

4. Experimental Section

Synthesis of PpIX-Loaded PSilQ NPs: The synthesis of PpIX-ligand (**1**) is described in the literature.[14] The fabrication of the PSilQ NPs was carried out through a reverse-microemulsion method.[26] An organic phase was prepared by mixing Triton X-100 (7.08 g, 6.6 mL), hexanol (6.4 mL), and cyclohexane (30.0 mL). At the same time, an aqueous phase was prepared by quickly dissolving PpIX ligand (**1**) (8 mg) in H_2O (5.6 mL) and NH_4OH (1.0 mL, 25% w/w). The aqueous phase was immediately added dropwise to the organic phase under stirring. This emulsion was stirred for 24 h at room temperature. Afterwards, the PSilQ NPs were obtained by precipitating out the material with the addition of ethanol (40.0 mL). The nanoparticles were separated from the solution by centrifugation. The nanoparticles were washed twice with ethanol to remove unreacted reagents and the final product was stored in the same solvent.

Functionalization of PSilQ NPs with Amino-Methoxypolyethylene Glycol (MeO-PEG-NH2) Polymer or NIR-Labeled PEG: The synthesis and characterization of MeO-PEG-NH_2- and NIR-797-labeled PEG-NH_2 is described in the Supporting Information. To functionalize the surface of PSilQ NPs with MeO-PEG-NH_2 (MW = 2 K), PSilQ NPs (10 mg) were

dispersed in dimethylformamide (DMF, 10 mL). To this dispersion, *N*-3-dimethylaminopropyl-*N*-ethylcarbodiimide (EDC, 25 mg, 0.13 mmol) and MeO-PEG-NH_2 (50 mg, 25 µmol) were added. The solution was stirred for 48 h at room temperature. The final PEG-PSilQ materials were collected by centrifugation, washed twice with ethanol, and stored in the same solvent.

For the in vivo experiments, NIR-797-labeled PEG was used to synthesize NIR-PEG-PSilQ NPs. PSilQ NPs (10 mg) were dispersed in DMF (10 mL). To this dispersion, EDC (0.13 mmol, 25 mg) and NIR-797-labeled PEG-NH_2 (50 mg, 17 µmol) prepared in situ (see Supporting Information) were added. The solution was stirred for 48 h at room temperature. The NIR-PEG-PSilQ NPs were collected by centrifugation and stored in ethanol.

Investigation of PSilQ NPs Degradability in Solution: The PSilQ NPs were dispersed in PBS at a concentration of 0.5 mg mL^{-1}. The hydrodynamic size (D_h) of this dispersion was taken as the reference point ($t = 0$). After that, the reducing agent DTT was dissolved in the nanoparticle dispersion under slow stirring at 37 °C for a final concentration of 10×10^{-3} M. Aliquots (1 mL) were taken at different time points (4, 24, and 48 h) for the analysis of D_h using DLS. A sample of PSilQ NPs in the absence of DTT was used as a control. The data are represented as PSD in volume (%) at different time points.

Release Profile of PpIX from PSilQ NPs: To determine the release of PpIX from PSilQ NPs under simulated reducing conditions, DTT was used. The PSilQ NPs were washed at least five times with DMF to eliminate any physisorbed porphyrin. The nanoparticles were redispersed in DMF (10 mL) at a concentration of 0.5 mg mL^{-1}. The dispersion was stirred for 19 h total under N_2 atmosphere to determine the quantity of background PpIX release. After the background was determined, DTT was dissolved in the dispersion to obtain a final concentration of 10×10^{-3} M. Aliquots were taken at different time points, centrifuged down, and the UV–vis absorption of the supernatant was measured at 408 nm to determine the amount of PpIX released. A similar procedure was followed for the control experiment that included PSilQ NPs in the absence of the reducing agent. The data are represented as percentage of PpIX released based on the total amount of PpIX loaded into the nanoparticles. The data are reported as the mean ± SD of three independent experiments.

Phototoxicity Studies: MDA-MB-231, MDA-MB-453, and MCF-7 cells were seeded at a density of 5×10^3 cells per well in a 96-well plate with 100 µL of media and incubated for 24 h at 37 °C under 5% CO_2 atmosphere. The cells were inoculated with PpIX, PSilQ NPs, or PEG-PSilQ NPs at equivalent concentrations ranging from 0.1×10^{-6} to 5.0×10^{-6} M of PpIX (Table S3, Supporting Information) and incubated for 72 h at 37 °C with 5% CO_2 atmosphere. As a control, PpIX was dispersed in media to obtain concentrations ranging from 0.1×10^{-6} to 5.0×10^{-6} M. After 72 h, the cells were washed twice with PBS and irradiated using a BioTable power source with RGB LED array (University of São Paulo, Brazil) at 630 nm for 20 min at 24.5 mW cm^{-2} (29.4 J cm^{-2}) in PBS. After irradiation, the PBS was removed, fresh complete media was added, and cells were incubated again at 37 °C with 5% CO_2 atmosphere. Irradiation was performed two more times at 4 and 8 h following the first irradiation, for a total fluence of 88.2 J cm^{-2}. After the final irradiation, fresh media was added to the cells and they were incubated for 24 h at 37 °C with 5% CO_2 atmosphere. Then, the cells were washed twice with PBS, and 120 µL of a 17% v/v CellTiter 96 solution in media was added. The cells were incubated for 3 h at 37 °C with 5% CO_2 atmosphere. After that, the absorbance was measured at 490 nm using a Multiskan FC plate reader. Cell viability (%) was calculated as follows: viability = ($A_{sample}/A_{control}$) × 100%, where A_{sample} and $A_{control}$ denote the absorbance values of the sample and of the control wells measured at 490 nm, respectively. The results are reported as the average ± SD of four experiments. The EC$_{50}$ values were determined using GraphPad Prism (v8.2.0 for Windows, La Jolla California, CA, USA) by fitting the cell viability data to a sigmoidal curve mathematical model.

In Vitro ROS Generation: MDA-MB-231 cells were seeded in a six-well plate at a concentration of 2×10^5 cells per well and incubated for 24 h at 37 °C with 5% CO_2 atmosphere. The cells were inoculated with PpIX, PSilQ, or PEG-PSilQ NPs at an equivalent concentration of 2×10^{-6} M PpIX, and incubated for 24 h at 37 °C with 5% CO_2 atmosphere. After that, the cells were washed twice with PBS, a 10×10^{-6} M solution of 2′,7′-

dichlorodihydrofluorescein diacetate (DCFH-DA) in serum-free media was added, and the cells were incubated for 30 min. The cells were washed again with PBS before irradiation using the BioTable at 630 nm for 20 min at 24.5 mW cm^{-2} (29.4 J cm^{-2}). Immediately after irradiation, the cells were washed with PBS and harvested using trypsin. The formation of 2′,7′-dichlorofluorescein was quantified by monitoring fluorescence at 528 nm using a flow cytometer (BD LSRFortessa cell analyzer). Cells not treated with nanoparticles, but incubated with ROS probe solution, were used as the control. The data are represented as percentage of cells DCF positive and are reported as the average ± SD of three independent experiments.

To further confirm the intracellular generation of ROS, confocal microscopy was used. MDA-MB-231 cells were seeded at a concentration of 5×10^4 cells per well on a glass cover slip in a six-well plate with 2 mL of complete media and incubated for 24 h at 37 °C with 5% CO$_2$ atmosphere. The cells were inoculated with PpIX, PSilQ, or PEG-PSilQ NPs at an equivalent concentration of 2×10^{-6} M PpIX and incubated for 24 h at 37 °C with 5% CO$_2$ atmosphere. The cells were washed twice with PBS and incubated with DCFH-DA probe solution (5×10^{-6} M, 1 mL) for 30 min at 37 °C with 5% CO$_2$ atmosphere. After incubation with the probe, the cells were washed twice with PBS. The cells were kept on PBS and irradiated using BioTable at 630 nm for 20 min at 24.5 mW cm^{-2} (29.4 J cm^{-2}). After irradiation, the PBS was removed and the glass cover-slips were mounted on a microscope slide using a spacer. Cells without any treatment, and cells treated with PpIX, PSilQ, or PEG-PSilQ NPs but not irradiated, were used as controls. The DCF-positive cells were imaged using an Olympus FluoView FV 1000 confocal microscope.

In Vitro Singlet Oxygen Generation: Intracellular $^1O_2$ generated by nanoparticles was quantified by an indirect method using the fluorescence from a $^1O_2$ probe, SOSG in the cell lysate.[14] MDA-MB-231 cells were seeded in a 96-well plate at a density of 5×10^3 cells per well and incubated for 24 h at 37 °C in 5% CO$_2$ atmosphere. The cells were treated with PpIX, PSilQ, or PEG-PSilQ NPs (2×10^{-6} M PpIX) and incubated for 48 h at 37 °C in 5% CO$_2$ atmosphere. After inoculation with nanoparticles, the cell media was removed, and the cells were washed twice with PBS to remove any non-internalized nanoparticles. Then, 100 µL PBS was added and the cells were lysed by adding 20 µL of 1% Triton X-100 to each well. The plates were incubated for 30 min at room temperature for complete cell lysis. Meanwhile, a stock solution of $^1O_2$ probe (5×10^{-3} M) was prepared by dissolving 100 µg of SOSG molecule in 33 µL of methanol. The SOSG stock solution was further diluted in PBS to afford a working solution of 50×10^{-6} M. After cell lysis, 12 µL of the working SOSG solution (50×10^{-6} M) was added to each well. The lysate-containing plates were irradiated with using BioTable at 630 nm for 20 min at 24.5 mW cm^{-2} (29.4 J cm^{-2}). The fluorescence of the lysates was measured at 505/520 nm (ex/em) using a microplate reader. Cells without any treatment and cells treated with PpIX, PSilQ, or PEG-PSilQ NPs but not irradiated were used as controls. The fluorescence intensity (FI) values obtained were used to calculate the relative FI (RFI) = (FI$_{sample}$ − FI$_{control}$)/FI$_{control}$, where FI$_{control}$ is measured for cells not treated with nanoparticles in the presence of SOSG. The results are reported as the average of relative fluorescence intensities (RFI) ± SD of three independent experiments.

Apoptotic Cell Determination Using Annexin-V Assay: MDA-MB-231 cells were seeded in a six-well plate at a concentration of 1×10^5 cells per well and incubated for 24 h at 37 °C in 5% CO$_2$ atmosphere. The cells were inoculated with the PpIX, PSilQ, or PEG-PSilQ NPs (4×10^{-6} M PpIX) and incubated for 48 h at 37 °C in 5% CO$_2$ atmosphere. After that, the cells were washed twice with PBS before irradiation using BioTable at 630 nm for 20 min at 24.5 mW cm^{-2} (29.4 J cm^{-2}). Then the PBS was removed, centrifuged, and stored to include the dead cells. The cells were replenished with fresh complete media and incubated at 37 °C in 5% CO$_2$ atmosphere. The irradiation was repeated two more times, at 4 and 8 h following the first irradiation, for a total fluence of 88.2 J cm^{-2}. After the final irradiation, the cells were replenished with fresh complete media and incubated for 12 h at 37 °C in 5% CO$_2$ atmosphere. After 12 h, the cells were washed with PBS, trypsinized, and centrifuged to collect the cell pellet. Then, the cell pellet was gently mixed with 1 mL of 1× binding buffer and centrifuged down. The cells were resuspended in 200 µL of binding buffer followed by the addition of 5 µL of Annexin V-FITC solution. The cell suspensions were incubated for 15 min at room temperature in the dark. Then, 700 µL of the binding buffer was added and the cells were centrifuged down. The cell pellet was resuspended in 200 µL of binding buffer and transferred to flow cytometry tubes. Then 5 µL of PI solution was added to each tube and incubated for 5–10 min at room temperature under dark. The cells were immediately analyzed using FACS. Cells without any treatment, and cells treated with PpIX, PSilQ, or PEG-PSilQ NPs but not irradiated, were used as controls. Cells that were both Annexin V-FITC and PI (FITC-/PI-) negative are considered healthy; Annexin V-FITC positive and PI negative (FITC+/PI–) cells are considered early apoptotic; cells that are positive for both Annexin V-FITC and PI (FITC+/PI+) are considered late-apoptotic; finally, Annexin V-FITC negative and PI positive (FITC–/PI+) are considered necrotic. The data are represented as apoptotic cells (early plus late-apoptotic cells) and necrotic cells. The results are reported as the average ± SD of three independent experiments.

All animal experiments were reviewed and approved by the University of North Carolina at Charlotte (Charlotte, NC) Institutional Animal Care and Use Committee under protocol (17-013) and followed the National Institutes of Health guide for the care and use of Laboratory animals (NIH Publications No. 8023, revised 1978). Female C57BL/6 and NOD SCID Gamma (NSG) mice were purchased from Jackson Laboratory.

Establishment of an Orthotopic Xenograft TNBC Model: Female NSG mice (6–8 weeks) were used to establish the TNBC orthotopic mice following a protocol already reported in the literature with slight modifications.[73] MDA-MB-231 cells (1×10^6) were mixed with Corning GFR reduced Matrigel (100 µL of 1:1 Matrigel/PBS), and implanted into the left fourth mammary fat pad of NSG mice. After cell implantation, the tumor growth was measured every alternate day using a caliper and tumor volume was calculated using the following formula ($\frac{l \times w^2}{2}$).[76] The tumors reached palpable sizes at 7 days, and ≈100 mm^3 after 14 days post-cell implantation.

Phototherapeutic Efficacy of PEG-PSilQ NPs: NSG mice bearing orthotopic tumors of ≈100 mm^3 were used for evaluating the phototherapeutic efficacy of PEG-PSilQ NPs. The mice were randomly divided into four groups ($n = 3$): PBS (control/dark, D), PEG-PSilQ NPs (dark, D), PpIX (light, L), and PEG-PSilQ NPs (light, L). The mice were intravenously injected using a retro-orbital injection with 50 mg kg^{-1} of PEG-PSilQ NPs and equivalent PpIX (2.1 mg kg^{-1}) solution in PBS (200 µL) for a total of five injections, with an interval of 4 days between injections (Figure 5). For the groups under light treatment, after each injection, there were three irradiation doses using the LINCE instrument at 24, 30, and 48 h post-injection with red light (630 nm, 125 mW cm^{-2}, 12 min, 90 J cm^{-2}). The timing and irradiation conditions were chosen based on the nanoparticle localization in the tumors and to prevent the formation of hypoxic environments in the tumors.[74] For all groups, the mice were kept under regular intervals of dark and light cycles in the vivarium −12 h under light and 12 h under dark conditions as recommended by the IACUC. The tumor growth was monitored using caliper, every other day, during the treatment process. The mice body weights were recorded every other day to keep track of any weight loss due to adverse effects. After the completion of five cycles of treatment, the mice were monitored for additional 2 days and the mice were sacrificed. All major organs, including tumors, were harvested and the tumors were weighed to corroborate the phototherapeutic efficacy. The organs were imaged using IVIS and sections of tissue samples were fixed for sectioning and histological examinations, as depicted in Supporting Information. The rest of the tissue samples were frozen and used later to determine the PpIX and Si content following the protocols described in the following two sections.

Analysis of PpIX Content in Major Organs and Tumor: The organ samples were weighed and placed in an extraction solution of 1% SDS in methanol/1N perchloric acid (1:1; v:v).[71] Each organ was homogenized using an IKA T-25 high-speed digital homogenizer until no solid pieces remained. The homogenized organ solution was incubated for 24 h to guarantee maximum extraction of PpIX from the tissue. After that, the solution was centrifuged and the supernatant was collected. The fluorescence of the supernatants was measured at 407/620 (ex/em) in a 96-well plate using fluorometer (SpectraMax M5, Molecular devices). The concentration

**ADVANCED
SCIENCE NEWS**

www.advancedsciencenews.com

**ADVANCED
THERAPEUTICS**

www.advtherap.com

of PpIX was determined by using a calibration curve with different concentrations of PpIX treated under similar conditions and reported as micrograms of PpIX per gram of organ. The results are reported as the average $\pm$ SD of organ samples from all the mice in a group ($n = 3$).

Analysis of Si Content in Major Organs and Tumor: Tissue samples were weighed and completely dried in an oven at 60 °C for 3 days. The dried organs were weighed and digested using a mixture of $HNO_3/HCl/HF$ (10:2:1). The samples were placed in the digestion vessels with the acid mixture for predigestion during 20 min at room temperature. The samples were then digested in a CEM Mars microwave system using the following conditions: ramp to 200 °C for 20 min, hold at 200 °C for 20 min, and cool down to room temperature. The digested samples were diluted to 50 mL using DI water. Finally, these samples were used for the Si content analysis using an ICP-OES system (PerkinElmer 8300 DV). Calibration standards were prepared by diluting Si element PlasmaCAL (SCP Science) standard in 0.1 M HNO_3. The wavelength of 251.66 nm was selected for Si analysis and the concentration was determined using Syngistix software. The data are represented as the milligrams of Si per gram of tissue. The results are reported as the average $\pm$ SD of organ samples from all the mice in a group ($n = 3$).

Statistical Analysis: All the data in the manuscript are represented as mean $\pm$ SD unless mentioned otherwise. For the nanoparticle size analysis using SEM, 160 nanoparticles were analyzed using ImageJ, and the size distribution is reported. The hydrodynamic size, ζ-potential, and nanoparticle degradation analysis using DLS were performed in triplicates. The amount of PpIX loaded, singlet oxygen generation, and PpIX release was analyzed in triplicates or more using different batches of nanoparticles. Cellular uptake using flow cytometry was evaluated with a minimum of 5000 gated cells. The cellular uptake, ROS, singlet oxygen generation, and apoptotic/necrotic cells were quantified in triplicates. The statistical analysis was performed with one-way ANOVA using Tukey's multiple comparison test. For the cell viability studies, the GraphPad prism was used to calculate the EC_{50} values ($n = 6$). All the in vivo experiments were evaluated using $n = 3$ mice per group. Statistical analysis for NIR/PpIX fluorescence data, Si, and PpIX content in organs was analyzed using two-way ANOVA using Tukey's multiple comparison test. The tumor volumes were reported as mean $\pm$ SEM, and two-way ANOVA with Tukey's multiple comparison test was used for statistical analysis. For tumor weights, unpaired t-test was performed to analyze the statistical difference of each group with respect to PBS group. All the statistical analyses were performed using GraphPad Prism (v8.2.0 for Windows) with $\alpha = 0.05$ and reported as stars assigned to the p-values; ****$p \leq 0.0001$, ***$p \leq 0.001$, **$p \leq 0.01$, *$p \leq 0.05$, and ns $p > 0.05$.

Supporting Information

Supporting Information is available from the Wiley Online Library or from the author.

[1] J. L. Vivero-Escoto, R. C. Huxford-Phillips, W. Lin, *Chem. Soc. Rev.* **2012**, *41*, 2673.
[2] J. G. Croissant, Y. Fatieiev, N. M. Khashab, *Adv. Mater.* **2017**, *29*, 1604634.
[3] P. Armanetti, S. Pocovi-Martinez, A. Flori, C. Avigo, D. Cassano, L. Menichetti, V. Voliani, *Nanomedicine* **2018**, *14*, 1787.
[4] D. Cassano, S. Pocovi-Martinez, V. Voliani, *Bioconjugate Chem.* **2018**, *29*, 4.
[5] A. Maleki, H. Kettiger, A. Schoubben, J. M. Rosenholm, V. Ambrogi, M. Hamidi, *J. Controlled Release* **2017**, *262*, 329.
[6] Y. Zhou, G. Quan, Q. Wu, X. Zhang, B. Niu, B. Wu, Y. Huang, X. Pan, C. Wu, *Acta Pharm. Sin. B* **2018**, *8*, 165.
[7] J. L. Paris, A. Baeza, M. Vallet-Regi, *Expert Opin. Drug Delivery* **2019**, *16*, 1095.
[8] S. P. Hadipour Moghaddam, R. Mohammadpour, H. Ghandehari, *J. Controlled Release* **2019**, *311–312*, 1.
[9] J. G. Croissant, X. Cattoen, J. O. Durand, M. W. C. Man, N. M. Khashab, *Nanoscale* **2016**, *8*, 19945.
[10] A. Noureddine, C. J. Brinker, *Chem. Eng. J.* **2018**, *340*, 125.
[11] J. G. Croissant, C. J. Brinker, *Enzymes* **2018**, *43*, 181.
[12] J. Della Rocca, M. E. Werner, S. A. Kramer, R. C. Huxford-Phillips, R. Sukumar, N. D. Cummings, J. L. Vivero-Escoto, A. Z. Wang, W. B. Lin, *Nanomedicine* **2015**, *11*, 31.
[13] J. G. Croissant, J. I. Zink, L. Raehm, J. O. Durand, *Adv. Healthcare Mater.* **2018**, *7*, e1701248.
[14] R. Juneja, Z. Lyles, H. Vadarevu, K. A. Afonin, J. L. Vivero-Escoto, *ACS Appl. Mater. Interfaces* **2019**, *11*, 12308.
[15] J. L. Vivero-Escoto, W. J. Rieter, H. Lau, R. C. Huxford-Phillips, W. Lin, *Small* **2013**, *9*, 3523.
[16] R. L. Yanovsky, D. W. Bartenstein, G. S. Rogers, S. J. Isakoff, S. T. Chen, *Photodermatol., Photoimmunol. Photomed.* **2019**, *35*, 295.
[17] X. Shi, C. Y. Zhang, J. Gao, Z. Wang, *Wiley Interdiscip. Rev.: Nanomed. Nanobiotechnol.* **2019**, *11*, e1560.
[18] J. P. Celli, B. Q. Spring, I. Rizvi, C. L. Evans, K. S. Samkoe, S. Verma, B. W. Pogue, T. Hasan, *Chem. Rev.* **2010**, *110*, 2795.
[19] R. Baskaran, J. Lee, S. G. Yang, *Biomater. Res.* **2018**, *22*, 25.
[20] A. E. O'Connor, W. M. Gallagher, A. T. Byrne, *Photochem. Photobiol.* **2009**, *85*, 1053.
[21] G. Yi, S. H. Hong, J. Son, J. Yoo, C. Park, Y. Choi, H. Koo, *Quant. Imaging Med. Surg.* **2018**, *8*, 433.
[22] M. Gift, K. Ann, I. Mfouo Tynga, H. Abrahamse, *Photodiagn. Photodyn. Ther.* **2018**, *22*, 147.
[23] W. G. Roberts, K. M. Smith, J. L. McCullough, M. W. Berns, *Photochem. Photobiol.* **1989**, *49*, 431.
[24] A. Ferrario, C. J. Gomer, *Cancer Res.* **1990**, *50*, 539.
[25] I. Mfouo Tynga, H. Abrahamse, *Nanomaterials* **2018**, *8*, 923.
[26] D. L. Vega, P. Lodge, J. L. Vivero-Escoto, *Int. J. Mol. Sci.* **2016**, *17*, 16.
[27] J. L. Vivero-Escoto, D. L. Vega, *RSC Adv.* **2014**, *4*, 14400.

[28] J. L. Vivero-Escoto, D. De Cillis, L. Fritts, D. L. Vega, *Proc. SPIE* **2014**, *8931*, 89310Z.

[29] Y. Fatieiev, J. G. Croissant, K. Julfakyan, L. Deng, D. H. Anjum, A. Gurinov, N. M. Khashab, *Nanoscale* **2015**, *7*, 15046.

[30] J. S. Suk, Q. Xu, N. Kim, J. Hanes, L. M. Ensign, *Adv. Drug Delivery Rev.* **2016**, *99*, 28.

[31] L.-C. Hu, M. Khiterer, S.-J. Huang, J. C. C. Chan, J. R. Davey, K. J. Shea, *Chem. Mater.* **2010**, *22*, 5244.

[32] V. Francia, K. Yang, S. Deville, C. Reker-Smit, I. Nelissen, A. Salvati, *ACS Nano* **2019**, *13*, 11107.

[33] I. T. Teng, Y. J. Chang, L. S. Wang, H. Y. Lu, L. C. Wu, C. M. Yang, C. C. Chiu, C. H. Yang, S. L. Hsu, J. A. Ho, *Biomaterials* **2013**, *34*, 7462.

[34] S. J. Lee, K. Park, Y.-K. Oh, S.-H. Kwon, S. Her, I.-S. Kim, K. Choi, S. J. Lee, H. Kim, S. G. Lee, K. Kim, I. C. Kwon, *Biomaterials* **2009**, *30*, 2929.

[35] L. Yan, J. Miller, M. Yuan, J. F. Liu, T. M. Busch, A. Tsourkas, Z. Cheng, *Biomacromolecules* **2017**, *18*, 1836.

[36] S. J. Lee, H. Koo, D. E. Lee, S. Min, S. Lee, X. Chen, Y. Choi, J. F. Leary, K. Park, S. Y. Jeong, I. C. Kwon, K. Kim, K. Choi, *Biomaterials* **2011**, *32*, 4021.

[37] S. Mura, J. Nicolas, P. Couvreur, *Nat. Mater.* **2013**, *12*, 991.

[38] Q. Tang, B. Yu, L. Gao, H. Cong, N. Song, C. Lu, *Curr. Med. Chem.* **2018**, *25*, 1837.

[39] V. P. Torchilin, *Nat. Rev. Drug Discovery* **2014**, *13*, 813.

[40] G. Saito, J. A. Swanson, K. D. Lee, *Adv. Drug Delivery Rev.* **2003**, *55*, 199.

[41] F. Q. Schafer, G. R. Buettner, *Free Radicals Biol. Med.* **2001**, *30*, 1191.

[42] M. P. Alvarez-Berrios, J. L. Vivero-Escoto, *Int. J. Nanomed.* **2016**, *11*, 6251.

[43] X. Zhang, K. Achazi, D. Steinhilber, F. Kratz, J. Dernedde, R. Haag, *J. Controlled Release* **2014**, *174*, 209.

[44] L. Gutierrez, S. Romero, G. B. da Silva, R. Costo, M. D. Vargas, C. M. Ronconi, C. J. Serna, S. Veintemillas-Verdaguer, M. Del Puerto Morales, *Biomed. Tech.* **2015**, *60*, 417.

[45] L. Yan, A. Amirshaghaghi, D. Huang, J. Miller, J. M. Stein, T. M. Busch, Z. Cheng, A. Tsourkas, *Adv. Funct. Mater.* **2018**, *28*, 1707030.

[46] D. van Straten, V. Mashayekhi, H. S. de Bruijn, S. Oliveira, D. J. Robinson, *Cancers* **2017**, *9*, 19.

[47] G. M. Calixto, J. Bernegossi, L. M. de Freitas, C. R. Fontana, M. Chorilli, *Molecules* **2016**, *21*, 342.

[48] R. R. Allison, C. Sibata, T. S. Mang, V. S. Bagnato, G. H. Downie, X. H. Hu, R. Cuenca, *Photodiagn. Photodyn. Ther.* **2004**, *1*, 157.

[49] M. J. Lamberti, N. B. R. Vittar, V. A. Rivarola, *World J. Clin. Oncol.* **2014**, *5*, 901.

[50] B. P. George, H. Abrahamse, *Anti-Cancer Agents Med. Chem.* **2016**, *16*, 793.

[51] D. Kessel, *Photochem. Photobiol.* **2019**, *95*, 119.

[52] P. Mroz, A. Yaroslavsky, G. B. Kharkwal, M. R. Hamblin, *Cancers* **2011**, *3*, 2516.

[53] I. O. Bacellar, T. M. Tsubone, C. Pavani, M. S. Baptista, *Int. J. Mol. Sci.* **2015**, *16*, 20523.

[54] D. K. Deda, C. Pavani, E. Carita, M. S. Baptista, H. E. Toma, K. Araki, *J. Biomed. Nanotechnol.* **2013**, *9*, 1307.

[55] M. Bostad, C. E. Olsen, Q. Peng, K. Berg, A. Hogset, P. K. Selbo, *J. Controlled Release* **2015**, *206*, 37.

[56] T. A. Theodossiou, C. E. Olsen, M. Jonsson, A. Kubin, J. S. Hothersall, K. Berg, *Redox Biol.* **2017**, *12*, 191.

[57] A. Aranda, L. Sequedo, L. Tolosa, G. Quintas, E. Burello, J. V. Castell, L. Gombau, *Toxicol. In Vitro* **2013**, *27*, 954.

[58] R. Ruiz-Gonzalez, R. Bresoli-Obach, O. Gulias, M. Agut, H. Savoie, R. W. Boyle, S. Nonell, F. Giuntini, *Angew. Chem., Int. Ed.* **2017**, *56*, 2885.

[59] S. Kim, M. Fujitsuka, T. Majima, *J. Phys. Chem. B* **2013**, *117*, 13985.

[60] A. P. Castano, T. N. Demidova, M. R. Hamblin, *Photodiagn. Photodyn. Ther.* **2004**, *1*, 279.

[61] C. S. Oliveira, R. Turchiello, A. J. Kowaltowski, G. L. Indig, M. S. Baptista, *Free Radicals Biol. Med.* **2011**, *51*, 824.

[62] C. A. Robertson, D. H. Evans, H. Abrahamse, *J. Photochem. Photobiol., B* **2009**, *96(1)*, 1.

[63] Z. Ji, G. Yang, V. Vasovic, B. Cunderlikova, Z. Suo, J. M. Nesland, Q. Peng, *J. Photochem. Photobiol., B* **2006**, *84*, 213.

[64] M. van Engeland, L. J. Nieland, F. C. Ramaekers, B. Schutte, C. P. Reutelingsperger, *Cytometry* **1998**, *31(1)*, 1.

[65] A. M. Rieger, K. L. Nelson, J. D. Konowalchuk, D. R. Barreda, *J. Visualized Exp.* **2011**, *50*, e2597.

[66] J. G. Croissant, Y. Fatieiev, A. Almalik, N. M. Khashab, *Adv. Healthcare Mater.* **2018**, *7*, 1700831.

[67] D. Dreau, L. J. Moore, M. P. Alvarez-Berrios, M. Tarannum, P. Mukherjee, J. L. Vivero-Escoto, *J. Biomed. Nanotechnol.* **2016**, *12*, 2172.

[68] J. G. Croissant, Y. Fatieiev, A. Almalik, N. M. Khashab, *Adv. Healthcare Mater.* **2018**, *7*, 1700831.

[69] S. P. Hadipour Moghaddam, J. Saikia, M. Yazdimamaghani, H. Ghandehari, *ACS Appl. Mater. Interfaces* **2017**, *9*, 21133.

[70] S. D. Li, L. Huang, *Mol. Pharmaceutics* **2008**, *5*, 496.

[71] J. Moan, L. W. Ma, A. Juzeniene, V. Iani, P. Juzenas, F. Apricena, Q. Peng, *Int. J. Cancer* **2003**, *103*, 132.

[72] C. A. Hudis, L. Gianni, *Oncologist* **2011**, *16*(S1), 1.

[73] E. Iorns, K. Drews-Elger, T. M. Ward, S. Dean, J. Clarke, D. Berry, D. El Ashry, M. Lippman, *PLoS One* **2012**, *7*, e47995.

[74] A. Master, M. Livingston, A. Sen Gupta, *J. Controlled Release* **2013**, *168*, 88.

[75] M. Sachar, K. E. Anderson, X. Ma, *J. Pharmacol. Exp. Ther.* **2016**, *356*, 267.

[76] M. M. Tomayko, C. P. Reynolds, *Cancer Chemother. Pharmacol.* **1989**, *24*, 148.